Open Access Earth System Science Data Discussions

Global climate-related predictors at kilometre resolution for the past and future

Philipp Brun[1], Niklaus E. Zimmermann[1], Chantal Hari[1,2,3,4], Loïc Pellissier[1,5], Dirk Nikolaus Karger[1]

[1] Swiss Federal Research Institute WSL, 8903 Birmensdorf, Switzerland

5   [2] Wyss Academy for Nature at the University of Bern, 3011 Bern, Switzerland

[3] Climate and Environmental Physics, Physics Institute, University of Bern, 3012 Bern, Switzerland

[4] Oeschger Centre for Climate Change Research, University of Bern, 3012 Bern, Switzerland

[5] Landscape Ecology, Institute of Terrestrial Ecosystems, Department of Environmental System Science, ETH Zürich, 8092 Zürich, Switzerland.

10 *Correspondence to*: Philipp Brun (philipp.brun@wsl.ch)

Abstract. A multitude of physical and biological processes on which ecosystems and human societies depend are governed by climatic conditions. Understanding how these processes are altered by climate change is central to mitigation efforts. Based on mechanistically downscaled climate data, we developed a set of climate-related variables at yet unprecedented spatiotemporal detail as a basis for environmental and ecological analyses. We created gridded data for near-surface relative

15 humidity (*hurs*), cloud area fraction (*clt*), near-surface wind speed (*sfcWind*), vapour pressure deficit (*vpd*), surface downwelling shortwave radiation (*rsds*), potential evapotranspiration (*pet*), climate moisture index (*cmi*), and site water balance (*swb*), at a monthly temporal and 30 arcsec spatial resolution globally, from 1980 until 2018 (time-series variables). At the same spatial resolution, we further estimated climatological normals of frost change frequency (*fcf*), snow cover days (*scd*), potential net primary productivity (*npp*), growing degree days (*gdd*), and growing season characteristics for the periods

20 1981-2010, 2011-2040, 2041-2070, and 2071-2100, considering three shared socioeconomic pathways (SSP126, SSP370, SSP585) and five Earth system models (projected variables). Time-series variables showed high accuracy when validated against observations from meteorological stations. Projected variables were also highly correlated to observations, although some variables showed notable biases, e.g., snow cover days (*scd*). Together, the CHELSA-BIOCLIM+ data set presented here (https://doi.org/10.16904/envidat.332, Brun et al., 2022) allows improving our understanding of patterns and processes

25 that are governed by climate, including the impact of recent and future climate changes on the world's ecosystems and associated services to societies.

1 Introduction

Climate change is impacting multiple facets of the Earth system with consequences on the functioning of natural ecosystems,
30   on the persistence of biological diversity, and on human societies (IPCC, 2022; IPBES, 2018). Climate regulates a broad
variety of processes on Earth, from purely physical ones, such as feeding rivers with precipitation or generating wind, which
are critical for renewable energy production (IPCC, 2011), to biological ones, such as fuelling ecosystem and agricultural
productivity (Howden et al., 2007), which sustain nearly all live on Earth, including humans (Bellard et al., 2012; Araújo and
Rahbek, 2006; Willis and Bhagwat, 2009). A sound understanding of how these processes and relationships are affected by
35   climate change is key. Among the important consequences of climate change are, for example, recent extreme weather events
and associated disturbances, such as floods, droughts, or wildfires, which have fostered studies that attempted to identify and
characterise the responsible climate signatures (Seneviratne et al., 2012; Zscheischler et al., 2018). Most of these disruptive
events can only be detected and analysed at high spatial and/or temporal resolutions and at a precise moment in space and time
(Easterling et al., 2000). In many regions of the world, existing climate time series lack such high resolution, and thus only to
40   a limited degree allow establishing an understanding of the underlying relationships between climate and the natural and human
system it interacts with (Easterling et al., 2016). By the end of the 21st century climate change is expected to lead to profound
changes in the distribution ranges of species and ecosystems (Thuiller et al., 2005, 2019). A reasonable anticipation of such
changes has to rely on sound information on climate-related variables, considering different climate-change scenarios. The
availability of relevant climate-related data at high spatiotemporal resolution for current conditions and for the decades ahead
45   of us is therefore crucial to fill the gaps in our understanding of climate-change impact on the Earth system.

A popular repository for climate data is hosted by the climatologies at high resolution for the Earth's land surface areas
(CHELSA) initiative (Karger et al., 2017, 2021c, 2020), which provides information on temperature and precipitation globally
at kilometre resolution. Originally, the CHELSA initiative offered climate data primarily as climatologies, i.e., as monthly and
seasonal statistics typically averaged over a representative period of 30 years or longer (Arguez and Vose, 2011), initially from
50   1979-2013. A key set of such climatologies are the 19 bioclimatic variables (Hijmans et al., 2005) that represent annual
statistics of precipitation and temperature and are widely used as predictors in macroecology. However, while these original
data may be relevant for many applications they have three primary limitations, they only: (1) include variables that
independently summarise either temperature or precipitation, (2) represent long-term climatic conditions, and (3) represent the
recent past.

55   For a sound understanding of how physical and biological processes are driven by climate, information on temperature and
precipitation alone is not sufficient. Assessing the potential for solar energy production, for example, is impossible without
knowing how much shortwave solar radiation (*rsds*) reaches a location of interest. Similarly, precipitation may measure the
amount of water that reaches the surface, but across the globe this is an inaccurate proxy for the amount of water that is
available to e.g. plants: 300 kg m^2 annual precipitation, for instance, can be found in the Alaskan taiga, in the Mongolian
60   steppe, or in the Pakistani desert (Karger et al., 2017), where the dominant vegetation exhibits large differences in the ability

to cope with water stress. Across these systems a much more accurate indicator of water stress is the climate moisture index (*cmi*, Hogg, 1997), i.e., the difference between precipitation and potential evapotranspiration (*pet*), as *pet* differs by a factor of three between the Alaskan taiga and the Pakistani desert (Singer et al., 2021). The popularity of the 19 bioclimatic variables to summarise climate therefore appears to result rather from the lack of relevant alternatives with kilometre-resolution than

65   from their imminent relevance.

Time-series data on climate-related variables are indispensable to understand the drivers of the many important Earth system processes that vary with time. Resolving how the primary weather patterns unfold, for example, allows for a much deeper understanding of the control of spatiotemporal patterns of ecosystem productivity (Hartman et al., 2020). Similarly, time-series of *pet* and *cmi* can be used to understand the country-wide temporal dynamics in crop yield (Zhang et al., 2015; Santini et al.,

70   2022). Modelling crop yields based on sound *pet* and *cmi* data may, in turn, allow for a better anticipation of shortages in food production and agricultural planning. Moreover, extreme weather events such as droughts can be identified and better linked to consequential disturbances like wildfires and forest diebacks. While for temperature and precipitation such time series of high temporal (daily) resolution data have recently been published (Karger et al., 2020, 2021c), global time-series at kilometre resolution are hardly available for other climate-related variables.

75   In order to anticipate and mitigate the manifold impacts of climate change until the end of this century, we also need future projections of meaningful climate-related variables. Climate change is expected to continue or even accelerate in the coming decades and its impacts on ecosystems and human societies are likely becoming stronger (IPCC, 2022). Crop yields, for example, are expected to change, tracking their optimal climate (Leng and Hall, 2019; IPCC, 2022): in high latitudes, harvests may become bigger due to warming, whereas elsewhere irrigation may become necessary to keep growing traditional crops.

80   In certain areas some crops will likely have to be abandoned entirely and replaced with better adapted alternatives. Such agricultural system changes are costly, take time, and are only efficient if the expected changes can be reasonably-well anticipated. Similarly, coping with the ongoing biodiversity crisis requires a rapid establishment of an optimally-designed global network of protected areas (Elsen et al., 2020; Hannah, 2008; Pollock et al., 2017). Yet, finding the most sustainable way to create such a network requires knowledge on the expected changes in climate and their impacts on the distribution

85   ranges of species. For temperature and precipitation, high-resolution future climatologies have been made available (Karger et al., 2017), but this is generally not the case for other climate-related variables that are more directly linked to ecosystem processes.

Here, we describe the CHELSA-BIOCLIM+ (Climatologies at high resolution for the Earth's land surface areas – bioclimatic variables plus) dataset of global kilometre-resolution time series and climatologies for 15 climate-related variables. We

90   compiled input data from CHELSA V.2.1 (Karger et al., 2021b) and other high-quality sources and used state-of-the art approaches to generate two groups of biologically relevant climate-related variables: for one group of variables we created time-series covering 39 years of the recent past (hereafter: time-series variables), and for the other group we created climatologies for current and expected future conditions (hereafter: projected variables). Time-series variables are available for the period of 1980-2018 and include near-surface relative humidity (*hurs*), cloud area fraction (*clt*), near-surface wind

95 speed (*sfcWind*), vapour pressure deficit (*vpd*), surface downwelling shortwave (solar) radiation (*rsds*), potential evapotranspiration (*pet*), and climate moisture index (*cmi*), each of which containing 468 monthly layers at a 30 arcsec resolution (i.e., less than 1 km), and an annual statistic, i.e., site water balance (*swb*), containing 38 annual layers. For all of these variables but site water balance, we further calculated climatologies monthly, annually, and for annual ranges and extrema for the period 1981-2010. Projected variables include frost change frequency (*fcf*), snow cover days (*scd*), potential

100 net primary productivity (*npp*), growing degree days (*gdd*), growing season length (*gsl*), growing season temperature (*gst*), and growing season precipitation (*gsp*), for which we calculated climatological means for the same kilometre-resolution grid for the periods 1981-2010, 2011-2040, 2041-2070, and 2071-2100. For the latter three periods, climatological values were generated for each combination of three shared socio-economic pathways (SSPs, O'Neill et al., 2014) and five Earth system models. To demonstrate the robustness of these variables, we validated them, where feasible, against global sets of observations

105 from meteorological stations. Together, our layers of climate-related variables allow the characterisation of each pixel of the life-supporting landmass on Earth far more comprehensively than would be possible from temperature and precipitation alone: for the recent decades with monthly resolution and until the end of this century as projected climatologies.

2 Material and Methods

110   We developed 15 climate-related variables that complement and build on existing products of the CHELSA initiative (Karger et al., 2017). We classified these variables into five orders, representing increasing degrees of abstraction from *in situ* measurements (Fig. 1). First-order variables are directly measurable properties, including near-surface temperature (daily means and extrema), precipitation rates, near-surface relative humidity, cloud area fraction, solar radiation, and near-surface wind speed. While downscaled climatologies and time-series of temperature and precipitation rates have been made available

115   previously (Karger et al., 2017, 2021c, 2020), here we generated corresponding layers for the remaining first-order variables total cloud cover (*clt*), near-surface (10m) wind speed (*sfcWind*), and near-surface relative humidity (*hurs*). Directly based on these first-order variables, we have generated time series and climatologies for six biologically meaningful second-order variables, including frost change frequency (*fcf*), snow cover days (*scd*), potential net primary productivity (*npp*), vapour pressure deficit (*vpd*), and surface downwelling shortwave radiation (*rsds*). In the same way, we have generated time series

120   and climatologies of four third-order climate variables (based on first and second order variables), including growing season length (*gsl*), growing season precipitation (*gsp*), and growing season temperature (*gst*), and potential evapotranspiration (*pet*), as well as one fourth and one fifth order variable, i.e., climate moisture index (*cmi*) and site water balance (*swb*), respectively.
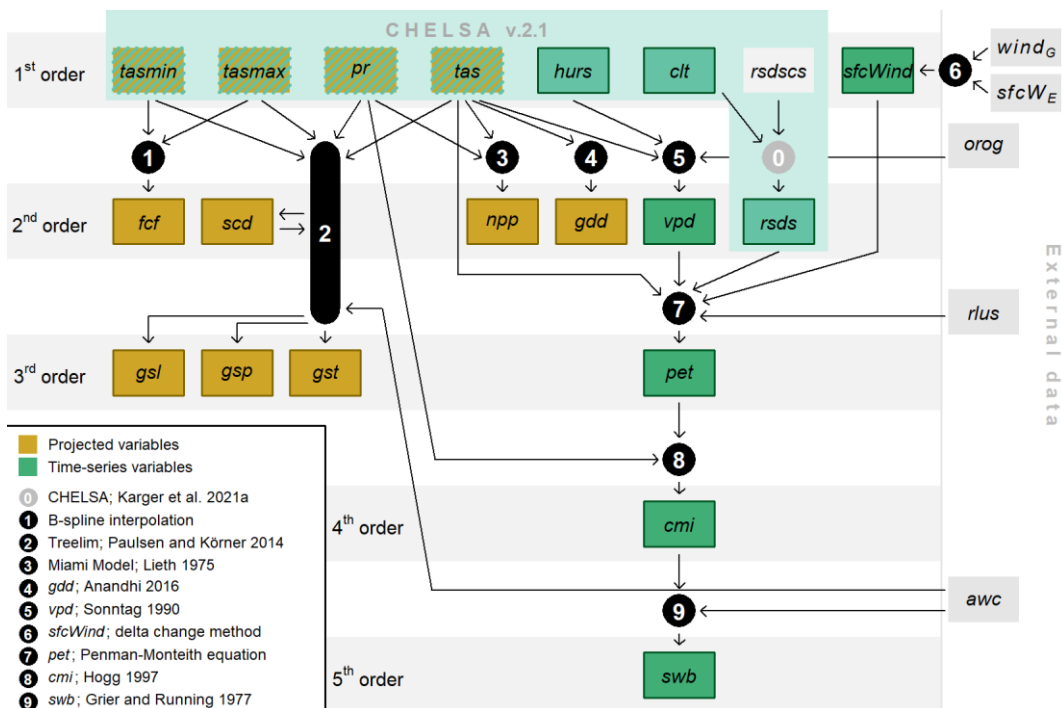
Figure 1: Input data, analyses, and output variables generated. *tasmin* **represents daily minimum near-surface air temperature;**
125   *tasmax* **represents daily maximum near-surface air temperature;** *pr* **represents precipitation rates;** *tas* **represents near-surface daily average air temperature;** *hurs* **represents near-surface relative humidity;** *clt* **represents cloud area fraction;** *rsdscs* **surface downwelling shortwave radiation assuming clear sky;** *orog* **represents orography;** *fcf* **represents frost change frequency;** *scd* **represents snow cover days;** *npp* **represents potential net primary productivity;** *gdd* **represents growing degree days;** *vpd* **represents vapour pressure deficit;** *rsds* **represents surface downwelling shortwave radiation corrected for atmospheric transmissivity and**

130   **topography; *sfcWind* represents near-surface wind speed; *sfcW$_E$* represents near-surface wind speed from ERA5; *wind$_G$* represents wind from Global Wind Atlas; *rlus* represents surface upwelling longwave radiation; *gsl* represents growing season length; *gsp* represents growing season precipitation; *gst* represents growing season temperature; *pet* represents potential evapotranspiration; *cmi* represents climatic moisture index; *awc* represents available soil water capacity; and *swb* represents site water balance. Green squares represent climate variables for which monthly time series are available for the period 1980-2018;**
135   **orange squares represent variables for which future projections of climatologies exist; hashed squares represent variables with both time series for the recent past and future projections. Squares with border lines are part of the data set presented.**

2.1. Input data

2.1.1 CHELSA data

Data on near-surface air temperature (*tasmin, tasmax, tas*), as well as precipitation rates (*pr*) and surface downwelling
140   shortwave radiation (*rsds*) have been taken from CHELSA V2.1 (Karger et al., 2021b). For past conditions, forcing from ERA5 (Hersbach et al., 2020) with a GPCC bias correction (Ziese et al., 2018) was used, as well as an air temperature algorithm that builds on an atmospheric lapse rate-based downscaling (Karger et al., 2017). Precipitation rates (*pr*) are based on a mechanistic downscaling that takes orographic effects into account (Karger et al., 2021c). Surface downwelling shortwave radiation (*rsds*) in CHELSA V2.1 based on a terrain-specific mechanistic model (Böhner and Antonic, 2009). For *tasmin*, *tasmax*, *tas*, and *pr*
145   we also used data on projected monthly climatologies for the periods 2011-2040, 2041-2070, and 2071-2100 from CHELSA V2.1. Such climatologies were generated for three official SSPs (O'Neill et al., 2016, 2017): SSP126 is an optimistic emission scenario, assuming that the world shifts gradually to a more sustainable path, resulting in additional radiative forcing of 2.6 W m^{-2} by 2100, relative to preindustrial levels; SSP370 is an intermediate-to-pessimistic scenario assuming that international fragmentation and a world characterised by regional rivalry hampers efficient implementations of globally sustainable
150   solutions, and thus additional radiative forcing to amount to 7.0 W m^{-2} by 2100; SSP585 is a pessimistic emission scenario, assuming that developing countries follow the trajectories of first world countries in rapid economic development that hardly relies on greenhouse gas-efficient technologies. It assumes additional radiative forcing of 8.5 W m^{-2} by 2100. For each of these SSPs, we used global simulations of five Earth system models that were prepared for the Intersectoral Impact Model Intercomparison Project round 3b (ISIMIP3b, https://www.isimip.org/) to generate future climatic anomalies of precipitation
155   and temperature. Earth system models were chosen based on the availability of all needed climate variables and model performance following ISIMIP3b (Lange, 2021) and included GFDL-ESM4 (Held et al., 2019), IPSL-CM6A-LR (Boucher et al., 2020), MPI-ESM 1-2-HR (Gutjahr et al., 2019), MRI-ESM2-0 (Yukimoto et al., 2019), and UKESM1-0-LL (Sellar et al., 2019). In a first step, for each variable (*tasmin*, *tasmax*, *tas*, and *pr*) the dynamic model outputs were used to generate monthly climatologies for the 3 periods × 3 SSPs × 5 Earth system models. In addition, for each Earth system model and climate
160   variable, one climatology was generated for the period 1981-2010. Then, each of these climatologies was downscaled to 30 arcsec using the delta-change method (Hay et al., 2000).

2.1.2 Other data

External data included data for orography (*orog*), wind speed (*windG*, *sfcW_E*), surface upwelling longwave radiation (*rlus*), and available soil water content (*awc*). Orography data originated from the Global Multi-resolution Terrain Elevation Data

165   2010 (GMTED2010; Danielson and Gesch, 2011) at a resolution of 30 arcsec. We obtained two types of wind speed data: long-term averages at high spatial resolution (9 arcsec), and monthly time-series at coarser spatial resolution. Wind speed averages for the period 2008-2017 at ten ($windG_{10}$) and 50 ($windG_{50}$) metres above surface were obtained from the Global Wind Atlas 3.0, a free, web-based application developed, owned and operated by the Technical University of Denmark (https://globalwindatlas.info). From these layers, we derived roughness length as

170   $$z_0 = e^{\frac{windG_{10}\ln(50) - windG_{50}\ln(10)}{windG_{10} - windG_{50}}}, \quad (1)$$

Then, we aggregated $windG_{10}$ and roughness length from the original 9 arcsec resolution to 30 arcsec, using a two-step approach. First, we aggregated to 27 arcsec (factor of three) by median, and then we resampled to 30 arcsec, using cell area-weighted means. Finally, in order to keep aggregated roughness length estimates in a realistic range and to remove a few outliers, we bounded them by the typical values for the open sea (0.0002) as minimum and city centres with

175   skyscrapers/mountain tops (4) as maximum (WMO, 2018). Monthly time-series of wind speed 10 m above the surface were obtained from the ERA5 global reanalysis product (*sfcW_E*, Hersbach et al., 2020) released by the European Centre for Medium-Range Weather Forecasts (ECMWF), and covered the period 1979-2020 with a horizontal resolution of 0.25°. Monthly information on the surface upwelling longwave radiation needed for the calculation of *pet* was obtained from the ERA5-Land reanalysis product (Muñoz Sabater, 2019; Muñoz-Sabater, 2021) that is also maintained by the ECMWF. It covered the period

180   1979-2020 with a horizontal resolution of 0.1°. Information on available soil water capacity (*awc*) was obtained from SoilGrids (Hengl et al., 2014, 2017) with a horizontal resolution of 30 arcsec and a vertical resolution of six soil layers. From these data, we calculated one layer of available water volume by integrating over the soil profiles.

2.2 Generating climate-related raster layers

2.2.1 First-order climate layers

185   **Near-surface relative humidity (*hurs*)**

Near-surface relative humidity (*hurs*) controls the biologically important variable vapour pressure deficit (see below) as well as fog formation (at *hurs* = 100 %), which can be a critical water source for vegetation in certain coastal ecosystems (e.g., in the California redwood forest; Dawson, 1998). We calculated *hurs* from atmospheric relative humidity (*hur*) at pressure levels *z* from ERA5 (Hersbach et al., 2020). We used all pressure levels from ERA5 and horizontally B-spline (S_{xy}) interpolated *hur*

190   at pressure levels $z_{i=1}...z_n$ to a 30 arcsec resolution, using longitude (*x*) and latitude (*y*) as predictors and *hur* as response, so that:

$$S_{xy}(hur) = f(x, y) \tag{2}$$

195 From the resulting spline-interpolated values $S_{xy}(hur)$ for each pressure level z, we then calculated a vertical spline interpolation separately for each 30 arcsec grid cell, using the geopotential height of each layer divided by the gravitational constant $g=9.80665$ m s^{-2} as predictor, and the values given by the function $S_{xy}(hur)$ as response so that:

$$S_z(hur) = S(S_{xy}(hur)) = f(z) \tag{3}$$

200

We then used the vertical spline $S_z(hur)$ to calculate a first approximation of $hurs_{orog}$ at the 30 arcsec, with $orog$ referring to surface altitude. This first approximation of the relative humidity at the surface, however, does not include orographic effects such as increased $hurs$ at windward and lower $hurs$ on leeward sides of an orographic barrier. Moist air is raising on the windward side of an orographic barrier, potentially losing moisture and cooling with a wet-adiabatic lapse rate, and sinking on

205 its leeward side, usually warming with a higher, dry-adiabatic lapse rate. This effect of differing adiabatic lapse rates and consequently temperature changes affects relative humidity. To include these orographic effects into the estimation of $hurs$, we use:

$$hurs = \frac{1}{(1+\exp(-1\cdot h))}, \tag{4}$$

210

with

$$h = \frac{h_t \cdot (H + (H_c - H)(1 - H_c))}{H_c}, \tag{5}$$

215 and h_t being the *logit*-transformed version of $hurs_{orog}$:

$$h_t = \log\left(\frac{hurs_{orog}}{1 - hurs_{orog}}\right), \tag{6}$$

H being the windward leeward index at 30 arcsec resolution calculated following the same parametrization as used in Karger

220 et al. (2021), and H_c being the spline-interpolated mean of all H values that overlap with the respective 0.25° grid cell from ERA5. We calculated $hurs$ monthly for the period 1980-2018. For the period 1981-2010, we derived monthly climatologies and climatological means, annual ranges and extrema. All $hurs$ data are reported as percentages.

Cloud area fraction (*clt*)

Earth System
Science
Data

Open Access   Discussions

225   The cloud area fraction (*clt*) represents the fraction of a grid cell that is covered by clouds across the entire atmospheric column, as seen from the surface or the top of the atmosphere. It includes both large-scale and convective clouds. Cloud area fraction determines the amount of downwelling solar radiation that reaches the Earth's surface and is an important constraint to productivity in tropical ecosystems (Nemani et al., 2003). Moreover, low-hanging clouds can be a key water source, and thus in mountain regions *clt* can be an important determinant of the distribution of tropical cloud forests (Karger et al., 2021d). We

230   calculated *clt* monthly for the period 1980-2018 following the procedure described in Karger et al. (in prep., 2021a). Unlike all other variables presented here, we downscaled *clt* to a cruder spatial resolution of 1.5 arcmin. For the period 1981-2010, we derived monthly climatologies and climatological means, annual ranges and extrema. All *clt* data are reported as percentages.

235   **Near-surface wind speed (*sfcWind*)**

Numerous direct and indirect effects of wind speed on terrestrial ecosystems exist, including gas and heat exchange, dispersal of pollen, seeds, pests or pollutants, and wind throw (Nobel, 1981). The impact of wind exposure on microclimate and vegetation patterns are particularly evident, for example, in the polar and subpolar zones (Schultz, 2005). We estimated monthly averages of near-surface (10 m) wind speed (*sfcWind*) at 30 arcsec resolution by downscaling and bias-correcting the

240   ERA5 time-series ($sfcW_E$), using an aggregation of the Global Wind Atlas product ($windG_{10}$; see subsection Input data). In a first step, we averaged $sfcW_E$ for the period 2008-2017, for which the Global Wind Atlas is representative. Then, we estimated the deviation between $sfcW_E$ and $windG_{10}$. We assumed *sfcWind* to follow a Weibull distribution (Weibull, 1951) and log-transformed wind speed estimates before calculating the difference between the $sfcW_E$ and $windG_{10}$. The resulting raster of differences contained information about both small-scale deviations from the ERA5 cell mean due to topography and bias in

245   long-term estimates of wind speed. We added this difference layer to each log-transformed, monthly ERA5 layer (from 1979-2019) and back-transformed the sum by exponentiating it. For the period 1981-2010, we derived monthly climatologies of *sfcWind* and climatological means, annual ranges and extrema. All *sfcWind* data are reported in metres per second.

2.2.2 Second-order climate layers

Frost change frequency (*fcf*)

250   Frost change frequency (*fcf*) describes the number of days per year with temperature minima below 0 °C and maxima above 0 °C. Coping with frost requires adapted behaviours or elaborate physiological adaptations for both ecto- and endothermal organisms, and especially for non-migrating life forms that cannot escape, such as plants. Frost change frequency carries information about the occurrence frequency of freezing and thawing events and - indirectly - about their duration, both of which are crucial constraints determining the best-suited adaptation strategies, see e.g., Hufkens et al. (2012). We used a B-

255   spline interpolation $S(tasmax, t)$ and $S(tasmin, t)$ to get both daily minimum ($tasmin_i$) and maximum ($tasmax_i$) near-surface 2 m air temperatures from monthly values, with t the sequence of Julian days marking the middle of each month, i.e., $[349, 15, 45, 74, 105, 135, 166, 196, 227, 258, 288, 319, 349, 15]$. As B-spline interpolations cannot predict values outside

their bounding knots, we first extended the sequence of knots to start at Dec. 15 (Julian day 349), and end at Jan. 15 (Julian day 15), and cut the interpolated sequence to range from Jan. 1 and Dec. 31 in a second step. A frost change event was then

260   defined by $tasmin_i < 0$ °C and $tasmax_i > 0$ °C. We calculated fcf from the monthly climatologies of $tasmin$ and $tasmax$ for the periods 1981-2010, 2011-2040, 2041-2070, and 2071-2100 for all combinations of SSPs and Earth System models (see subsection Input data). fcf is reported as the number of days per year with frost change events.

Snow cover days (scd)

Snow cover days (scd) are the number of days per year on which the ground is covered with snow. Snow cover affects local

265   climate, hydrology, and ecosystems in complex ways (Callaghan et al. 2011, Schultz 2005), by insulating the soil from temperature minima during winter months (Zhang, 2005), by determining Arctic vegetation patterns (Evans et al., 1989), or by providing hiding opportunities form predators for small mammals (Callaghan et al., 2011). We used a B-spline interpolation $S(tas, t)$ to get from monthly to daily estimates of tas, with t being a vector of Julian days marking the middle of each month, i.e., $[349, 15, 45, 74, 105, 135, 166, 196, 227, 258, 288, 319, 349, 15]$, and tas being the mean of near-surface 2 m air

270   temperature for the respective month. We used a stepwise interpolation of monthly precipitation rates to daily precipitation rates following Paulsen and Körner (2014). The daily precipitation rate (pr) in this approach is directly coupled to the near-surface air temperature as follows:

$$pr = \begin{cases} 5\,kg \cdot m^{-2} \cdot day^{-1} & if\ tas < 5°C \\ 10\,kg \cdot m^{-2} \cdot day^{-1} & if\ \ 5°C \leq tas < 10°C \\ 15\,kg \cdot m^{-2} \cdot day^{-1} & if\ \ 10°C \leq tas < 15°C \\ 20\,kg \cdot m^{-2} \cdot day^{-1} & if\ \ 15°C \leq tas \end{cases} \tag{7}$$

275

The total amount of pr is distributed to as many rainfall events as are necessary to obtain the monthly amount of precipitation, with events being evenly distributed across the month. Precipitation is solid (snow) when $tas < 0$ °C and accumulates as long as tas remains below 0 °C. If $tas > 0$ °C it melts by a rate of 0.84 kg m^{-2} day^{-1} K^{-1} (Paulsen and Körner, 2014). When liquid precipitation falls on an existing snow layer, it cools to 0 °C and the thermal energy released (4.186 kJ kg^{-1} K^{-1}) is assumed to

280   melt snow (Körner et al., 2011). The number of snow cover days (scd) is then given by the days of the year on which a snow layer with a snow water content of $\geq$ 1 kg m^{-2} existed. We calculated scd from the monthly climatologies of tas and pr for the periods 1981-2010, 2011-2040, 2041-2070, and 2071-2100 for all combinations of SSPs and Earth System models (see subsection Input data). scd is reported as the number of days per year with snow cover.

Potential net primary productivity (npp)

285   Potential net primary productivity (npp) is the potential difference between the rate at which carbon is fixed by photoautotrophs and the rate at which carbon is emitted through cell respiration, if only climate was limiting. Primary productivity is the main way through which carbon dioxide is removed from the atmosphere and biomass is produced and thus a key ecosystem function (Schimel, 1995). Here, we used the Miami model (Lieth, 1975) to estimate npp solely based on climatic constraints, resulting

in a potential estimate that is independent of the existing vegetation on the ground. The unit of *npp* is given as g m^{-2} yr^{-1}, where

290   g stands grams of dry matter. The estimates are based on mean annual near-surface 2 m air temperature in °C and annual

precipitation rates in kg m^{-2} yr^{-1}. The Miami model assumes that *npp* increases asymptotically with both increasing temperature

and increasing precipitation, approaching an upper limit of 3000 g m^{-2} yr^{-1}. The precipitation component to *npp* is given as

$$npp_{pr} = 3000 \times (1 - exp(-0.000664 \times pr)), \tag{8}$$

and the air temperature component is given as

295    $$npp_{tas} = 3000 \times (1 + exp(1.315 - 0.119 \times tas))^{-1} \tag{9}$$

Based on these two components, *npp* is either limited by temperature or precipitation, and determined by the minimum estimate

of *npp* from either the temperature or the precipitation component:

$$npp = min(npp_{tas}, npp_{pr}) \tag{10}$$

We calculated *npp* from the monthly climatologies of *tas* and *pr* for the periods 1981-2010, 2011-2040, 2041-2070, and 2071-

300   2100 for all combinations of SSPs and Earth System models (see subsection Input data).

Growing degree days (*gdd*)

Growing degree days (*gdd*) are a measure of heat accumulation over a specific time period. It has been used to understand the

phenology of plants and animals for centuries in agronomy (Anandhi, 2016), and for a shorter period in ecology (Cayton et

al., 2015). It has been shown that the heat sum above a critical threshold accumulated through time better explains e.g. plant

305   phenology than a threshold temperature alone (Larcher, 1994). The *gdd* threshold temperature ascertains that cool periods,

during which phenological progress stagnates, are omitted. The threshold temperature is species-specific, and varies e.g.

between 0 °C for cold-adapted plants (Larcher, 1994) to 5 or 5.5 °C for many temperate to boreal tree species (Prentice et al.,

1992; Lenihan, 1993), while tropical plants are limited by temperatures below 10 °C and even much higher (Larcher, 1994).

Growing degree days are calculated by first assessing whether daily mean near-surface 2 m air temperatures surpass a baseline

310   threshold temperature tas_b (e.g., 5 °C), and then summing all the surpluses. To obtain daily estimates of near-surface 2 m air

temperature from monthly values we have used the same approach of B-spline interpolation as for snow cover days. The

growing degree sum is then given as the sum:

$$gdd_b = \sum_{i=1}^{365}(max(tas_i - tas_b, 0)), \tag{11}$$

where tas_b is the baseline temperature and i represents Julian day. We calculated *gdd* for three baseline temperatures (0 °C, 5

315   °C, and 10 °C) from the monthly climatologies of *tas* for the periods 1981-2010, 2011-2040, 2041-2070, and 2071-2100 for

all combinations of SSPs and Earth System models (see subsection Input data). However, here we only report the results for

gdd with the 5 °C baseline (*gdd₅*). All *gdd* data are reported as degree days (°C day).

Vapour pressure deficit (*vpd*)

Vapour pressure deficit (*vpd*) is the difference between the actual amount of moisture in the air and the maximum amount of

320   moisture the air can hold at a given temperature. *vpd* is a key meteorological property for terrestrial biomes, determining plant functioning and drought-induced mortality (Grossiord et al., 2020). Moreover, the distributions of animals prone to dessication such as small arthropods are limited by *vpd* (Hauser et al., 2018; Ouisse et al., 2016). Near-surface *vpd* can be calculated from near-surface relative humidity (*hurs*), considered as unitless fraction, and near-surface air temperature (*tas*) in °C as

$$vpd = e_{sat}(tas) \times (1 - hurs), \tag{12}$$

325   where $e_{sat}(tas)$ is the saturation vapour pressure. In order to approximate $e_{sat}(tas)$, we used the Magnus equation with the coefficients of Sonntag (1990),

$$e_{sat}(tas) = 0.6112 \times e^{\frac{17.62*tas}{(243.12+tas)}}, \tag{13}$$

vpd was calculated in the R environment (R Development Core Team, 2008), using the package bigleaf (Knauer et al., 2018). We calculated vapour pressure deficit monthly for the period 1980-2018. For the period 1981-2010, we derived monthly

330   climatologies and climatological means, annual ranges and extrema. All *vpd* data are reported in Pascal (Pa).

Surface downwelling shortwave radiation (*rsds*)

Surface downwelling shortwave radiation (*rsds*) is the amount of direct and diffuse shortwave radiation that reaches the Earth's surface, considering the filtering effects of air and clouds throughout the atmosphere, as well as the effects of the local topography. *rsds* describes the amount of solar energy available. It can critically affect local climate and vegetation patterns

335   in high-latitude environments (Andrade et al., 2018; Schultz, 2005). In the tropics with year-round rain, where temperature and precipitation are not limiting, it can constrain primary productivity (Nemani et al., 2003). To calculate *rsds*, surface downwelling solar radiation under clear sky conditions (*rsdscs*) is first calculated by computing 30-arcsec clear-sky radiation using the method described in Böhner and Antonic (2009) for each day of the year. Then daily estimates of *rsdscs* and *clt* are combined through the following relationship:

340

$$rsds = rsdscs \cdot 1 - 0.75 \cdot clt^{3.4} \tag{14}$$

This way, daily estimates of *rsds* from 1980 to 2018 were generated in a related project (Karger et al., in prep.). Here, we summarised these estimates to monthly means, and for the period 1981-2010 we derived monthly climatologies and

345   climatological means, annual ranges and extrema. All *rsds* data are reported as MJ m^{-2} day^{-1}.

2.2.3 Third-order climate layers

Growing season-related predictors

The growing season is the annual period, during which conditions are favourable for vegetation growth. Growing season length (*gsl*) indicates the amount of time available for plant growth, which is an important determinant of life-history traits and

350 productivity (Paulsen and Körner, 2014). As *gdd*, *gsl* is species specific and can vary considerably between plants adapted to different biomes. Here, we estimate *gsl* for tree species forming treelines, i.e., growing at the cold/dry boundary of forested biomes worldwide. Under such conditions *gsl* can be defined as the number of days per year with temperatures > 0.9 °C, with no snow cover being present, and with sufficient water available in the soil (Paulsen and Körner, 2014). Daily precipitation rates and near-surface 2 m air temperature averages were calculated in the same way as for snow cover. In addition, potential

355 evapotranspiration was estimated, using the Hargreaves equation and *tasmin* and *tasmax* as input (Hargreaves and Samani, 1985). Note that this estimate of *pet* is specific to the estimate growing season-related predictors and independent of the more sophisticated approach presented below. Water balance in the soil was calculated by a two-layer bucket model. The upper layer is assumed to be able to hold 30 kg of liquid water per square metre at maximum. For the lower layer we used empirical data on water holding capacity *awc* (see Input data). Liquid precipitation, or snow melt fills the upper layer first. If the soil

360 water content of the upper layer (swc_1) exceeds 30 kg m^{-2}, water flows to the lower layer until saturated. If the second layer is saturated, the remaining flux is assumed to be lost as runoff. If water is present in the upper layer, actual evapotranspiration (*aet*) is equal to *pet*. We used a square-root correction for the estimation of the actual daily evapotranspiration from deeper layers as soon as the upper layer was empty: $aet = pet \times (swc_2/awc)^{1/2}$ in kg m^{-2} day^{-1}, with soil water given in kg m^{-2}. A growing season day is defined as a day on which $swc_1 > 0$ & *tas* > 0.9 °C & snow < 1 kg m^{-2}. Growing season length is then

365 the number of days per year on which this condition holds true, growing season precipitation (*gsp*) is the amount of precipitation (solid and liquid) that falls during the days on which the condition is true, and growing season temperature (*gst*) is the mean near-surface air temperature during days on which the condition is true. We calculated *gsl*, *gsp*, and *gst* from the monthly climatologies of *tasmin*, *tasmax*, *tas*, *pr*, and from the climatological means of *scd* for the periods 1981-2010, 2011-2040, 2041-2070, and 2071-2100 for all combinations of SSPs and Earth System models (see subsection Input data).

370 **Potential evapotranspiration (*pet*)**

Potential evapotranspiration (*pet*) is defined as the amount of water per area and time that could evaporate at the soil surface or be transpired through plants if soil water availability was not limiting. Evapotranspiration is a crucial part of the water cycle and strongly interacts with vegetation traits such as leaf area (Irmak, 2008). We calculated *pet* with the Penman-Monteith equation (Monteith, 1965) as implemented in the R package bigleaf (function 'potential.ET'). This function builds on the

375 following equation (Knauer et al., 2018):

$$\lambda E_{pot} = \frac{\Delta(R_n - G - S) + \rho \times c_p \times vpd \times Ga}{\Delta + \gamma(1 + \frac{Ga}{Gs_{pot}})}, \qquad (15)$$

where Δ is the slope of the saturation vapour pressure curve [kPa K^{-1}] that is approximated with equation 3; R_n is net radiation

380 [W m^{-2}]; G is the ground heat flux [W m^{-2}]; S is the sum of all storage fluxes [W m^{-2}]; ρ is the mean air density [kg m^{-3}]; c_p is

the specific heat of the air [J K^{-1} kg^{-1}]; γ is the psychrometric constant [kPa K^{-1}], Ga is the aerodynamic conductance [m s^{-1}]; and Gs_{pot} is the potential surface conductance [mol m^{-2} s^{-1}]. To calculate *pet* with the bigleaf framework, information on the following general environmental conditions is required: *tas*, *vpd*, R_n, pressure, *G*, and *S*. For *tas*, we used monthly layers of the CHELSA *tas* product (see Input data). For *vpd*, we used the layers calculated in this analysis. R_n was calculated as the

385 difference between surface downwelling shortwave radiation (*rsds*) calculated here, and surface upwelling longwave radiation (*rlus*) from ERA5-Land, following Singer et al. (2021). Since these radiation layers had different spatial resolutions (30 arcsec and 0.1°, respectively), we used the grid calculus tool of the System for Automated Geoscientific Analyses (SAGA, Conrad et al., 2015) to calculate the differences on the fine grid, using bilinear interpolation to downscale the coarse grid of *rlus*. In a few pixels (in rugged terrain) estimates of R_n could be negative, in which case we manually set them to zero. Pressure was

390 calculated with the function 'pressure.from.elevation' of the R package bigleaf (Knauer et al., 2018), considering orography, *tas*, and *vpd* as driving factors. Ground heat flux (*G*) was assumed to correspond to 10 % of R_n (Allen et al., 1998; Singer et al., 2021) and storage fluxes (*S*) were assumed to sum to zero.

In addition to general environmental conditions, information on aerodynamic and potential surface conductance were needed to calculate *pet* with the Penman-Monteith equation, and these metrics depend on the property of the surface considered. We

395 estimated conductances for a reference crop of 12 cm height, using the simplified relationships provided by (Allen et al., 1998). Ga was estimated as $\frac{w_{2*}}{208}$, with w_{2*} being wind speed two metres above roughness length [m s-1]. We derived w_{2*} from our monthly estimates of *sfcWind* (which are estimated 10 m above the surface) in the following way:

$$w_{2*} = sfcWind \times \frac{ln(\frac{z_0+2}{z_0})}{ln(\frac{10}{z_0})}, \tag{16}$$

400

where z_0 is roughness length (see subsection Input data). Gs_{pot} was calculated assuming a constant surface resistance of 70 s m^{-1} (Allen 1998) and considering local *tas* and pressure (using the bigleaf function 'ms.to.mol'). We calculated *pet* monthly from 1979 to 2019. For the period 1981-2010, we derived monthly climatologies of *pet* and climatological means, annual ranges and extrema. All *pet* data are reported as kg m^{-2} month^{-1}.

405 **2.2.4 Fourth-order climate layers**

Climate moisture index (*cmi*)

Climate moisture index (*cmi*) is the difference between precipitation and potential evapotranspiration (Hogg, 1997). *cmi* informs about the moisture regime and has been related to biome boundaries, and drought impact on tree health and regeneration (Hogg et al., 2017; Hogg, 1997). We calculated *cmi* for each month of the period 1980-2018, using the CHELSA

410 *pr* layers and the *pet* layers generated in this study. For the period 1981-2010, we derived monthly climatologies of *cmi* and climatological means, annual ranges and extrema. All *cmi* data are reported as kg m^{-2} month^{-1}.

2.2.5 Fifth-order climate layers

Site water balance (swb)

Site water balance (*swb*) is an estimate of the water available to plants during a year, which considers soil parameters in
415   addition to climate variables. *swb* has been shown to tightly correlate with functional plant traits such as leaf area (Grier and
Running, 1977; Gholz, 1982), and it is considered one of the main determinants of plant distribution (Neilson, 1995;
Woodward, 1987). We used an approach similar to that of Grier and Running (1977) to calculate site water balance. From the
cmi climatologies we identified the start of the hydrological year, i.e., either the first month after the arid period (with negative
cmi) or the month after the one with the lowest *cmi*. Then, monthly estimates of *cmi* are summed over the hydrological year,
420   whereby the running sum is never allowed to exceed the available water volume of the soil (approximated here by *awc*, see
Input data), and excess water is assumed to run off. When *pet* exceeds precipitation (negative *cmi*) the difference is subtracted
from the water balance, which often leads to significantly negative values over the course of a hydrological year. We calculated
swb for each year of the period 1980-2018, i.e., choosing 1981 as the first representative year and allowing hydrological years
to start in 1980 already. For the period 1981-2010, we derived climatological means. All *swb* data are reported as kg m^{-2} year^{-1}
425   .

2.3 Validation

We validated eight of the 15 climate-related variables, using global sets of station measurements. We validated primarily
variables that could either be measured directly or derived readily from measurements, using two different data sources. *clt*,
sfcWind, *fcf*, *scd*, and *gdd$_5$* were validated against the Global Historical Climatology Network Daily (GHCN-D) dataset, a
430   dataset containing meteorological, station-based measurements across the global land areas (Menne et al., 2012). All
validations based on the GHCN-D observations were made for climatologies of the period 1981-2010. For the validation of
cloud area fraction, the GHCN-D average observed cloudiness from midnight to midnight (ACMH) was used, while *sfcWind*
was compared to average daily wind speed measurements (AWND). *scd* was validated against snow depth (SNWD), whereby
daily observations with a snow depth exceeding 0.1 mm were considered as snow cover days and summed over the year. For
435   the validation of frost change frequency, daily GHCN-D maximum temperature (TMAX) and minimum temperature (TMIN)
were extracted. All days with temperature minima below 0 °C and maxima above 0 °C were summed to obtain the number of
days with frost changes per year. Growing degree days were calculated from the GHCN-D average temperature (TAVG). All
days with TAVG surpassing the 5 °C baseline temperature were identified and their surpluses aggregated to yearly degree-day
sums. The validation data were converted to the same units as the downscaled layers generated here, aggregated for each
440   station to monthly climatologies, and then compared to the corresponding pixels of the downscaled layers.

The variables *hurs, vpd*, and *pet* were compared with the World-wide Agroclimate Data of FAO (FAOCLIM, FAO, 2001).
This agro-climatic database contains monthly climatologies for 28,800 stations for 14 observed and computed agro-climatic
parameters. For the validation process, FAOCLIM version 2 was used, which covers the period 1961-1990, thus only partially

overlapping with our 1981-2010 climatologies or timeseries. The monthly climatologies of potential evapotranspiration and

445 relative humidity could directly be extracted from FAOCLIM, while vapour pressure deficit had to be calculated from relative humidity and mean temperature, as we did for the corresponding downscaled layers (see above). As for validations against the GHCN-D database, we converted the validation data to the same units and matched them with the downscaled layers. For all validated variables we report Pearson correlation coefficients (r), mean absolute errors (MAE), root mean squared errors (RMSE), absolute biases, and number of stations with validation data.

450 In addition to these validation results, we report spatial and temporal patterns for each variable. We show global maps as well as fine-scale patterns for one of two selected regions. Furthermore, for time-series variables we report seasonal and long-term variations for different biomes, as defined by Schultz (2005), and for projected variables we show differences between the climatological means for 1981-2010 and 2071-2100, assuming an SSP370 pathway and considering the MPI-ESM 1-2-HR model.

2.4 Output format and file organization

All downscaled layers are provided as georeferenced tiff files (GeoTIFF). GeoTIFF is a public domain metadata standard which allows georeferencing information to be embedded within a TIFF file. Identical to the CHELSA layers (Karger et al., 2017), maps are projected in World Geodetic System 1984 (EPSG 4326), and have a west extent of −180.0001388888°, a south extent of −90.0001388888°, an east extent of 179.9998611111° and a north extent of 83.9998611111°. Their resolution

460 is 0.0083333333° (30 arcsec), resulting in raster sizes of 20'880×43'200 cells. All GeoTIFF files are saved as integers with the compression option 'deflate', and an internal scale and offset (see Technical Specifications document on the CHELSA website). In order to read offset and scale correctly the geospatial data abstraction library (GDAL, https://gdal.org) version 2.2 or higher is needed, otherwise they may have to be applied manually. All variables are time-averages either representing the periods 1981-2010, 2011-2040, 2041-2070, or 2071-2100 (in case of climatologies) or individual year-month combinations

465 (in case of time series-data). Monthly time series range at least from 1980 to 2018 while the annual time series of *swb* ranges from 1981 to 2018. Climate variable and time period, as well as SSP and Earth system model (if applicable) are encoded in the file names.

2.5 Software used

For the generation and validation of the climate layers we relied on three open-source software environments. Most raster

470 operations, such as averaging or calculating extrema were executed with SAGA V.8.1 (Conrad et al., 2015); output GeoTIFFs were created with GDAL (https://gdal.org); and validation, visualisation, as well as complex raster operations were implemented in the R environment (R Development Core Team, 2008). R packages used, in addition to those indicated above, included sp (Pebesma and Bivand, 2005) raster (Hijmans, 2019), and magick (Ooms, 2020).

3 Results

3.1 Spatiotemporal patterns

3.1.1 First-order climate layers

Near-surface relative humidity (*hurs*) was highest in polar regions and - to a lesser extent - at the equator, and lowest in parts of the subtropics including northern Africa, the Arabian Peninsula and northwest Australia (Figure 2a). The seasonal variation of *hurs* was most pronounced in the far north, for example in northern Canada, but also along an east-west belt in subtropical Africa, from Ethiopia to Sierra Leone (Figure 2b). In terms of northern-hemisphere biomes, *hurs* was lowest in the dry tropics and subtropics, especially in May and June, and highest in the polar and subpolar zone, especially in January and February (Figure 2c). Over the past forty years, annual means of *hurs* varied in all northern-hemisphere biomes with consistent and clear trends of decreasing *hurs* (Figure 2d). In the northeastern boundary region of the Andes, *hurs* tended to be higher at the northern edge of the Andes and around the eastern mountain tops than in the eastern lowlands and on the Andean plateau (Figure 2e).
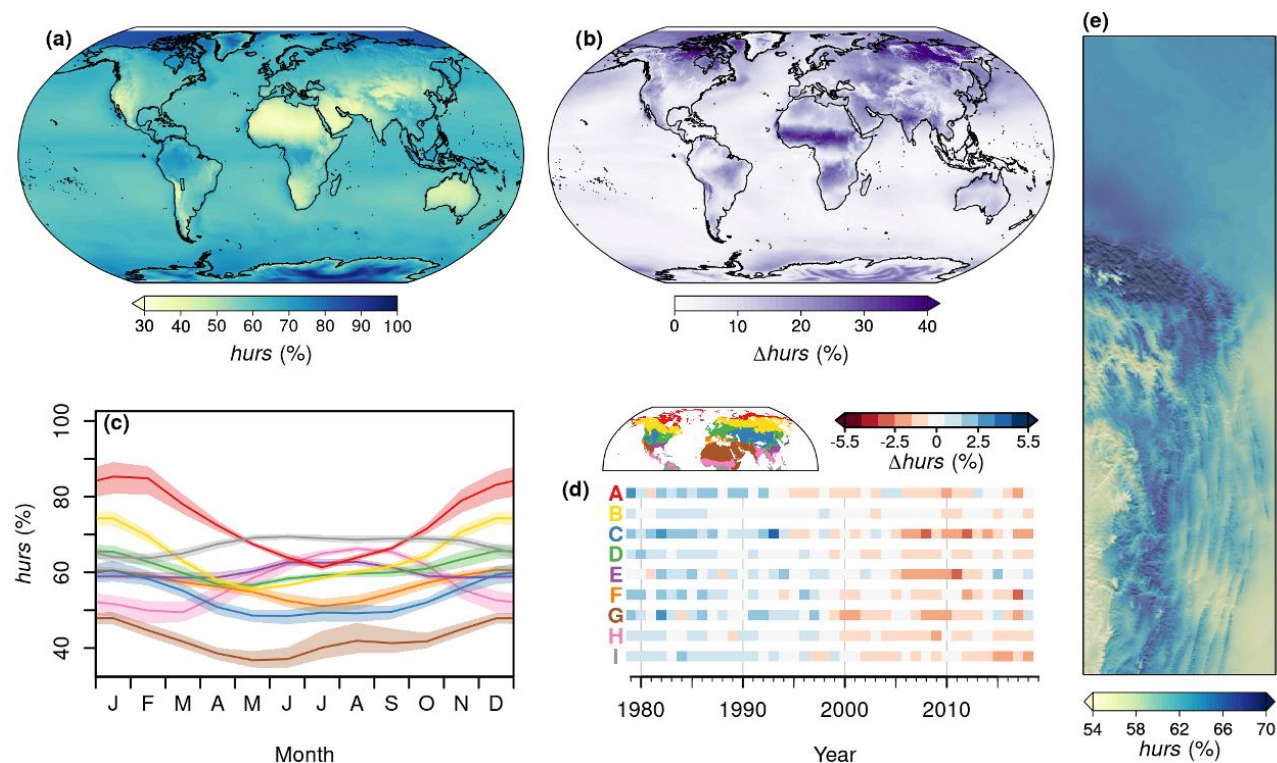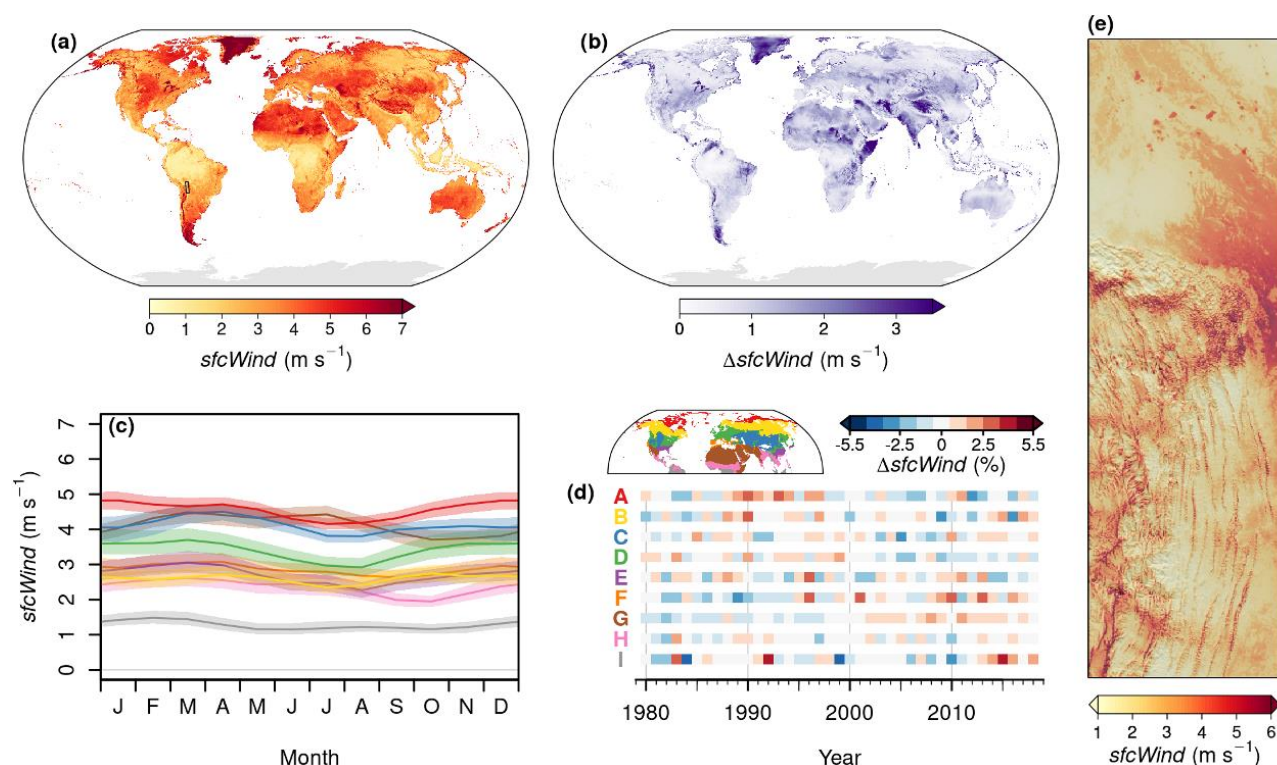

Figure 2: Overview over the spatiotemporal distribution of near-surface relative humidity (*hurs*): a, global map of the climatological mean for the period 1981-2010; b, global map of the range (max - min) of monthly *hurs* means for the period 1981-2010; c, seasonal cycle of *hurs* in the biomes of the northern hemisphere for the period 1981-2010. Polygons indicate the range from the fortieth to the sixtieth percentile, lines indicate medians. d, temporal change of annual mean *hurs* by biome. Shown are deviations in percent of the long-term (1979-2018) annual mean. Red (A) represents the polar and subpolar zone; yellow (B) represents the boreal zone; blue (C) represents dry midlatitudes; green (D) represents temperate midlatitudes; purple (E) represents subtropics with year-round rain; orange (F) represents subtropics with winter rain; brown (G) represents dry tropics and subtropics; pink (H) represents tropics

Earth System
Science
Data

Open Access

Discussions

495 with summer rain; and grey (I) represents tropics with year-round rain. e, an exemplary high-resolution map of the climatological mean of *hurs* for the northeastern boundary region of the Andes. For exact location see inset in panel (a).

Cloud area fraction (*clt*) was highest in polar regions and in some equatorial regions, such as Indonesia, and lowest in parts of the subtropics, including northern and South Africa and the Arabian Peninsula (Figure 3a). The seasonal variation of *clt* was most pronounced in subtropical and monsoon regions, for example on the Indian subcontinent (Figure 3b). In terms of northern-hemisphere biomes, *clt* was lowest in the dry tropics and subtropics, especially from June to August, and highest in the polar

500 and subpolar zone, especially in May and October (Figure 3c). Over the past forty years, substantial variations in annual mean *clt* were observed in most northern-hemisphere biomes with more (e.g., temperate midlatitudes) or less (e.g., dry tropics and subtropics) apparent negative trends (Figure 3d). In the northeastern boundary region of the Andes *clt* tended to be higher at the northern edge of the Andes and around the eastern mountain tops than in inner alpine valleys and on the Andean plateau (Figure 3e).

505
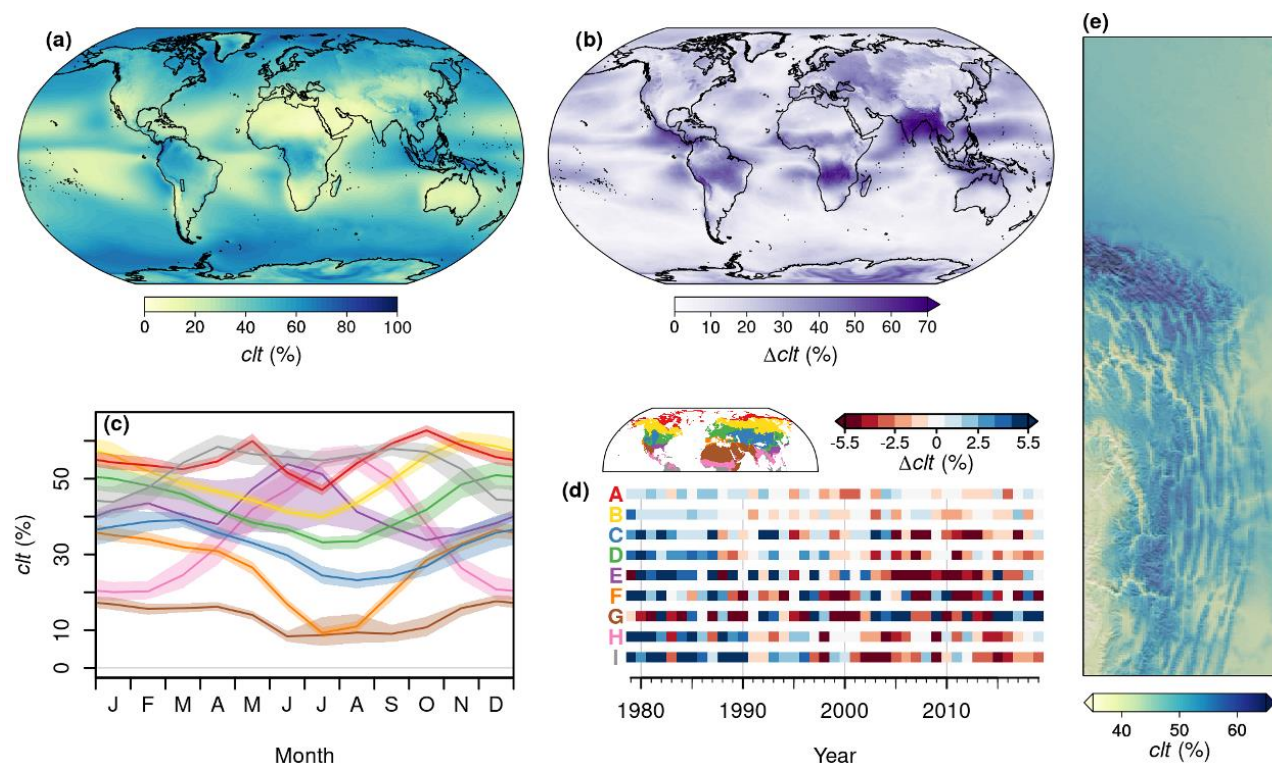
Figure 3: Overview over the spatiotemporal distribution of cloud area fraction (*clt*): a, global map of the climatological mean for the period 1981-2010; b, global map of the range (max - min) of monthly *clt* means for the period 1981-2010; c, seasonal cycle of *clt* in the biomes of the northern hemisphere for the period 1981-2010. Polygons indicate the range from the fortieth to the sixtieth percentile, lines indicate medians. d, temporal change of annual mean *clt* by biome. Shown are deviations in percent of the long-term
510 (1979-2019) annual mean. Red (A) represents the polar and subpolar zone; yellow (B) represents the boreal zone; blue (C) represents dry midlatitudes; green (D) represents temperate midlatitudes; purple (E) represents subtropics with year-round rain; orange (F) represents subtropics with winter rain; brown (G) represents dry tropics and subtropics; pink (H) represents tropics with summer rain; and grey (I) boundary region of the Andes. e, an exemplary high-resolution map of the climatological mean of *clt* for the northeastern boundary region of the Andes. For exact location see inset in panel (a).

515 Near-surface wind speed (*sfcWind*) was comparably high in the high latitudes, in coastal regions, in deserts and in mountain systems and lowest at the equator (Figure 4a). In general, seasonal variations were relatively small, with notable exceptions of seasonally variable *sfcWind* regions in a few, scattered regions such as Greenland and the horn of Africa (Figure 4b). In terms of northern-hemisphere biomes, *sfcWind* was lowest in the tropics with year-round rain and highest in the polar and subpolar zone (Figure 4c). Over the past forty years, substantial variations in annual mean *sfcWind* were observed in northern-

520 hemisphere biomes, yet without clear temporal trends (Figure 4d). However, *sfcWind* did show a tendency to increase in the dry tropics and subtropics and a tendency to decrease in the temperate midlatitudes. In the northeastern boundary region of the Andes, *sfcWind* tended to be highest on mountain tops, in the mideastern lowlands around the city of Santa Cruz de la Sierra, and above the lakes in the northern lowlands of the Amazon basin (Figure 4e).

525 **Figure 4: Overview over the spatiotemporal distribution of near-surface wind speed (*sfcWind*): a, global map of the climatological mean for the period 1981-2010; b, global map of the range (max - min) of monthly *sfcWind* means for the period 1981-2010; c, seasonal cycle of *sfcWind* in the biomes of the northern hemisphere for the period 1981-2010. Polygons indicate the range from the fortieth to the sixtieth percentile, lines indicate medians. d, temporal change of long-term (1980-2018) annual mean *sfcWind* by biome. Shown are deviations in percent of the annual mean. Red (A) represents the polar and subpolar zone; yellow (B) represents**
530 **the boreal zone; blue (C) represents dry midlatitudes; green (D) represents temperate midlatitudes; purple (E) represents subtropics with year-round rain; orange (F) represents subtropics with winter rain; brown (G) represents dry tropics and subtropics; pink (H) represents tropics with summer rain; and grey (I) represents tropics with year-round rain. e, an exemplary high-resolution map of the climatological mean of *sfcWind* for the northeastern boundary region of the Andes. For exact location see inset in panel (a).**

3.1.2 Second-order climate layers

535 Frost change frequency (*fcf*) was highest along a circumpolar belt in the temperate to high latitudes of the northern hemisphere (Figure 5a), as well as in some mountain systems such as the Andes, while it was zero across most of the subtropics and tropics. Until 2071-2100 *fcf* is expected to decrease in particular in global mountain systems and across much of the northern half of the contiguous United States, central and eastern Europe, and southwest Asia, while increasing frost change frequencies are expected for southeastern Canada, the baltic countries, Belarus, Ukraine, and in Mongolia, Northern and Northeastern China

540 and especially in the Hengduan and Himalaya mountains (Figure 5b), indicating an increase in thawing events in these areas. In the western Himalayas, *fcf* was highest at intermediate elevations, and it showed a tendency to decrease towards valley bottoms as well as towards mountain peaks (Figure 5c).
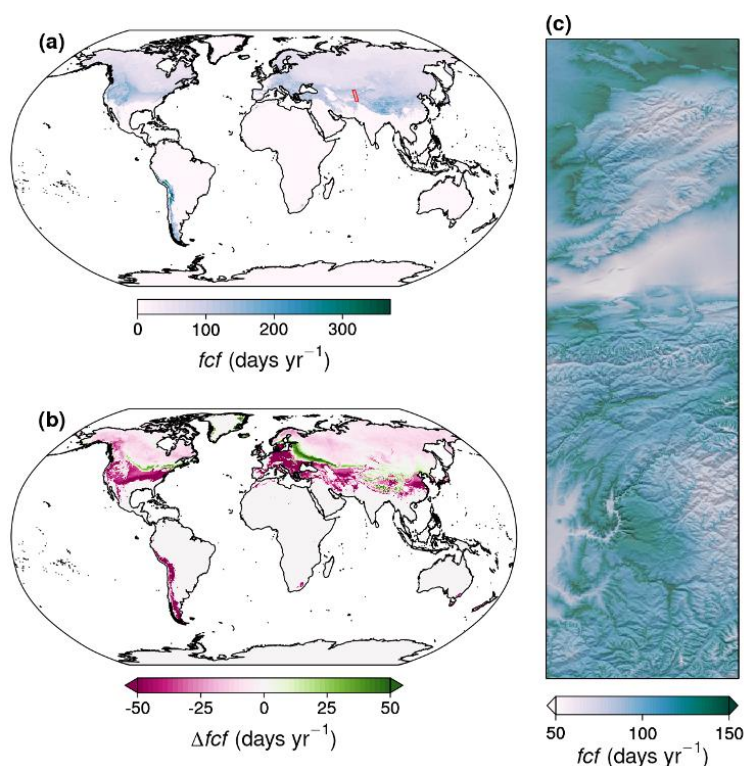
Figure 5: Overview over the spatiotemporal distribution of frost change frequency (*fcf*): a, global map of the climatological mean of
545 ***fcf* for the period 1981-2010; b, global map of the difference between climatological means of 2071-2100 and 1981-2010, assuming anthropogenic emissions to follow the shared socio-economic pathway SSP370 and building on projections of the Max Planck Institute Earth System Model (MPI-ESM 1-2-HR); c, an exemplary high-resolution map of the climatological mean for the western edge of the Himalayas. For exact location see inset in panel (a).**

Snow cover days (*scd*) increased with latitude, with zero *scd* occurring across most of the subtropics and tropics, except for
550 some mountain systems, e.g., the Himalayas (Figure 6a). Until 2071-2100 *scd* are expected to decrease in all regions of the world that currently have snow cover days, except for Greenland and Antarctica. Strongest declines are expected for the

northeastern contiguous United States and for eastern and northern Europe (Figure 6b). In the western Himalayas *scd* was positively associated with elevation (Figure 6c).
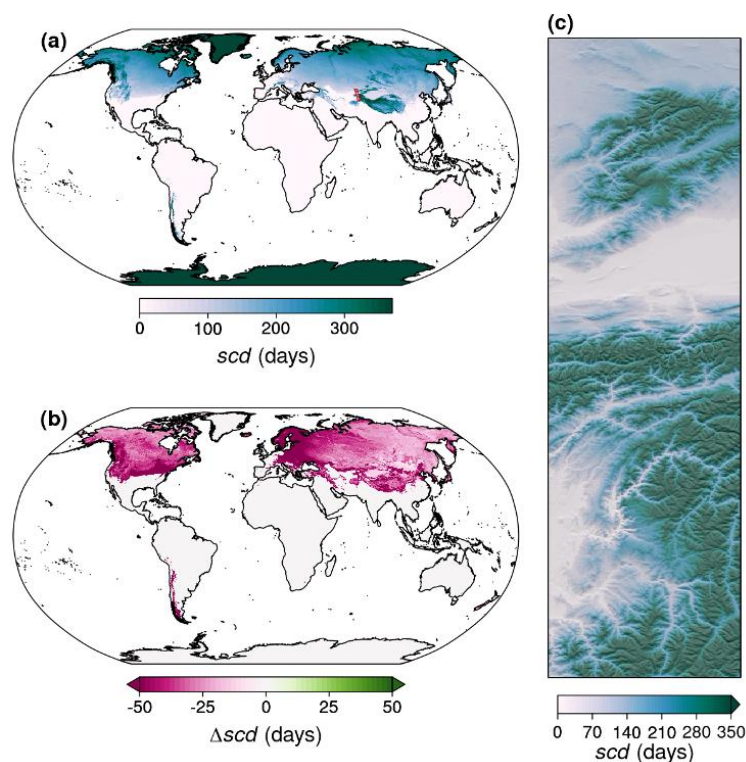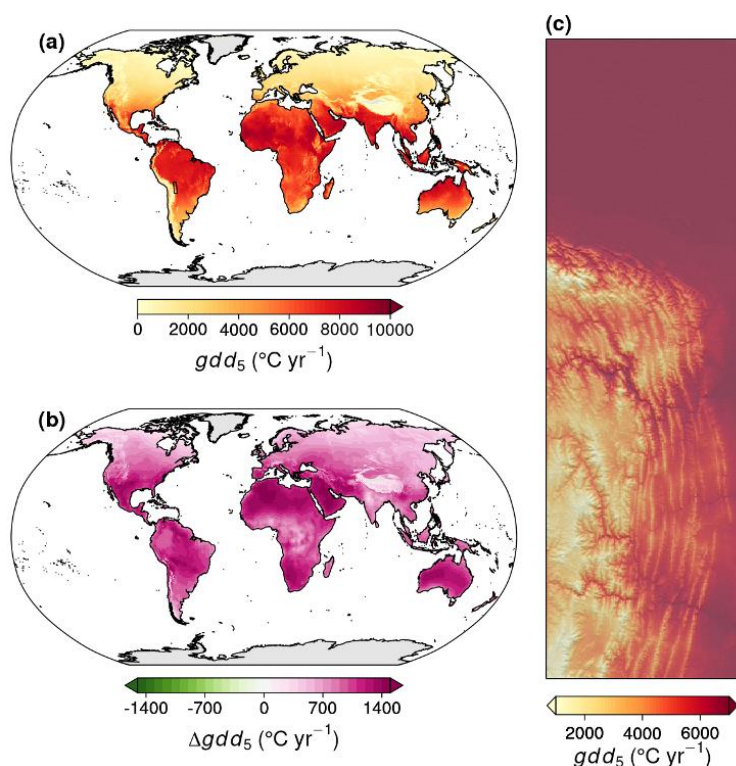

Figure 6: Overview over the spatiotemporal distribution of snow cover days (scd): a, global map of the climatological mean of scd for the period 1981-2010; b, global map of the difference between climatological means of 2071-2100 and 1981-2010, assuming anthropogenic emissions to follow the shared socio-economic pathway SSP370 and building on projections of the Max Planck Institute Earth System Model (MPI-ESM 1-2-HR); c, an exemplary high-resolution map of the climatological mean for the western edge of the Himalayas. For exact location see inset in panel (a).

Potential net primary productivity (*npp*) was highest in the tropics, for example in the Amazon Basin, and lowest close to the poles and in arid regions, such as northern Africa (Figure 7a). Until 2071-2100 *npp* is expected to increase across much of the northern high latitudes, in high mountain systems, and in the northwest of the Indian subcontinent. Decreasing *npp* is expected for the islands and the southern coast of the Caribbean Sea, Central America, and for the coasts of the Mediterranean Sea (Figure 7b). In the northeastern boundary region of the Andes, *npp* was highest in the northern lowlands of the Amazon Basin and lowest on the bottoms of dry inner-alpine valleys (Figure 7c).
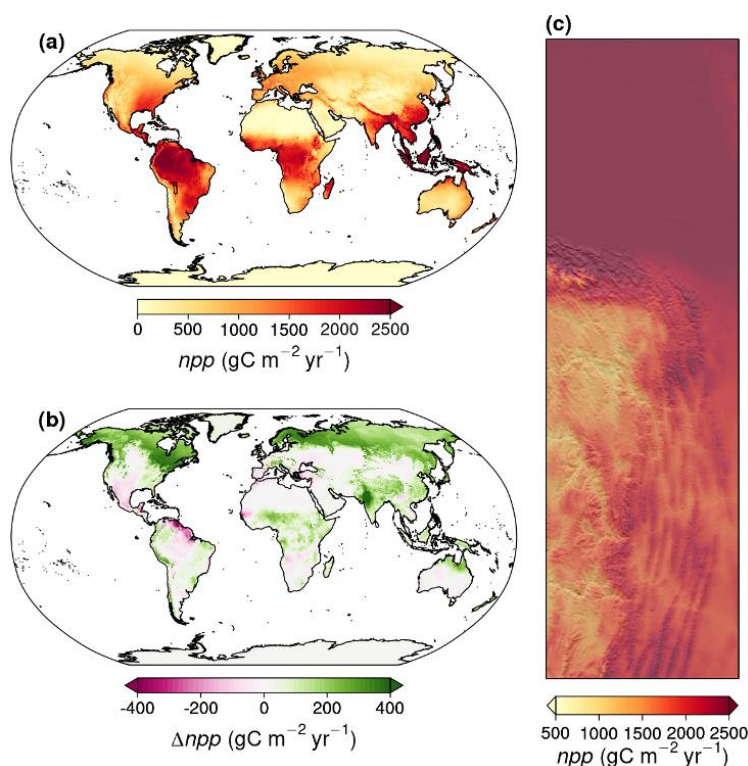
Figure 7: Overview over the spatiotemporal distribution of net primary productivity (*npp*): a, global map of the climatological mean of *npp* for the period 1981-2010; b, global map of the difference between climatological means of 2071-2100 and 1981-2010, assuming anthropogenic emissions to follow the shared socio-economic pathway SSP370 and building on projections of the Max Planck Institute Earth System Model (MPI-ESM 1-2-HR); c, an exemplary high-resolution map of the climatological mean for the northeastern boundary region of the Andes. For exact location see inset in panel (a).

Growing degree days with 5 °C baseline temperature (*gdd*$_5$) were highest in the tropics and subtropics and decreased towards the high latitudes (Figure 8a). Until 2071-2100 *gdd*$_5$ is expected to increase in all regions of the world, except for Greenland and Antarctica. Strongest increases are expected for northern Africa and the Arabian Peninsula, Mexico, and western Australia (Figure 8b). In the northeastern boundary region of the Andes, *gdd*$_5$ were highest in the northern lowlands of the Amazon basin and in some inner alpine valleys, while they were lowest on high mountain peaks and the Andean plateau (Figure 8c).

Figure 8: Overview over the spatiotemporal distribution of growing degree days with 5 °C baseline temperature (gdd_5): a, global map of the climatological mean of gdd_5 for the period 1981-2010; b, global map of the difference between climatological means of 2071-2100 and 1981-2010, assuming anthropogenic emissions to follow the shared socio-economic pathway SSP370 and building on projections of the Max Planck Institute Earth System Model (MPI-ESM 1-2-HR); c, an exemplary high-resolution map of the climatological mean for the northeastern boundary region of the Andes. For exact location see inset in panel (a).

The climatological mean of vapour pressure deficit (*vpd*) was highest in dry subtropical regions, for example northern Africa, the Arabian Peninsula, and Central and Western Australia. It was lowest in high mountain systems, such as the Himalayas, and polar regions (Figure 9a). The spatial patterns of seasonal variation in *vpd* were similar to those of the climatological mean (Figure 9b). In terms of northern-hemisphere biomes, *vpd* was lowest in the polar and subpolar zone, primarily from November to March, and highest in the dry tropics and subtropics, especially around June (Figure 9c). Over the past forty years annual mean *vpd* showed clearly increasing trends in all northern-hemisphere biomes (Figure 9d). In the northeastern boundary region of the Andes *vpd* showed a primary negative association with elevation, with highest *vpd* in the lowlands and in some inner alpine valleys and lowest *vpd* on mountain peaks and on the Andean plateau (Figure 9e).
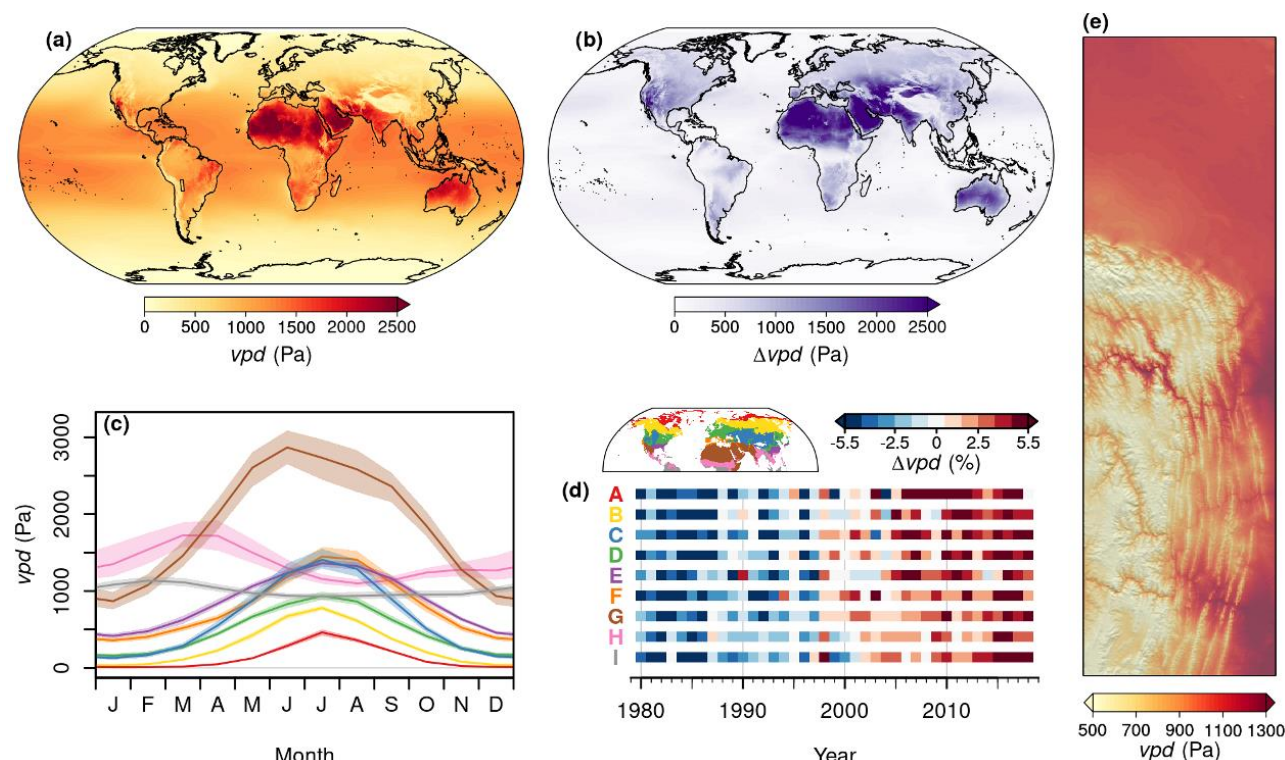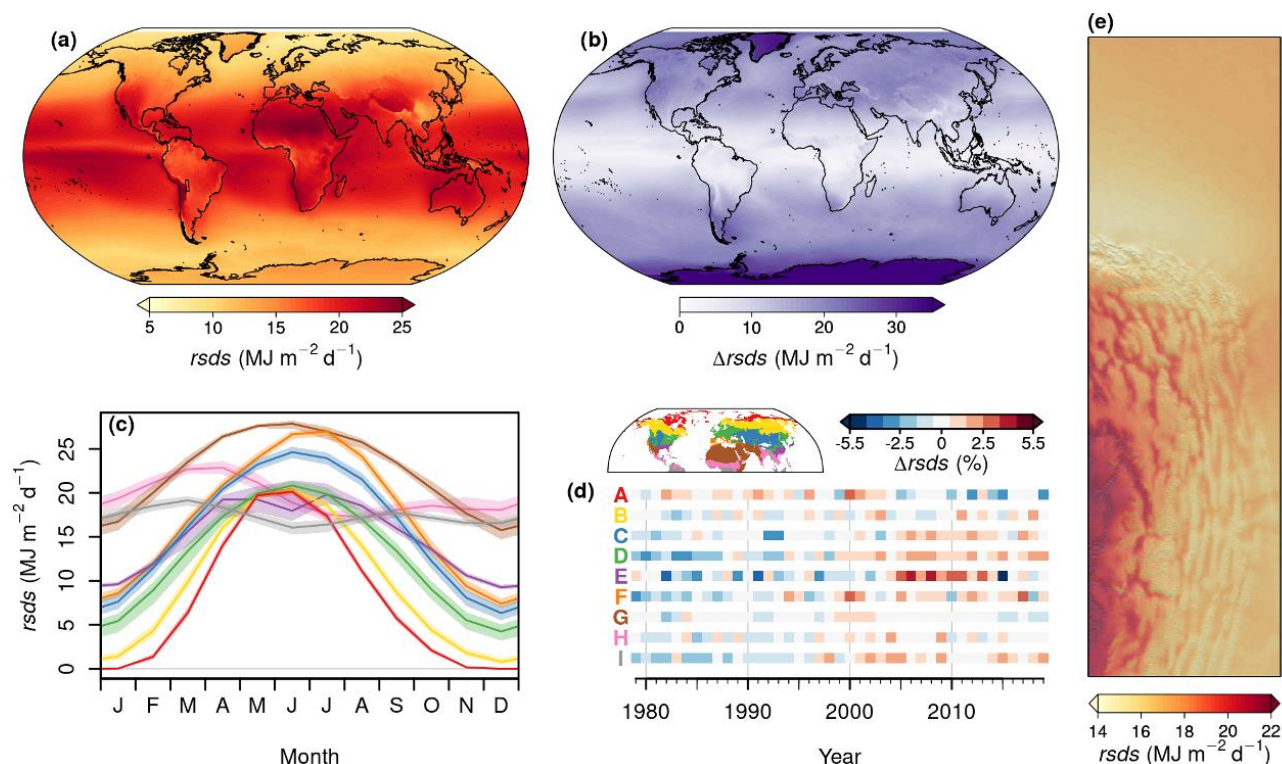
Figure 9: Overview over the spatiotemporal distribution of vapour pressure deficit (*vpd*): a, global map of the climatological mean for the period 1981-2010; b, global map of the range (max - min) of monthly *vpd* means for the period 1981-2010; c, seasonal cycle of *vpd* in the biomes of the northern hemisphere for the period 1981-2010. Polygons indicate the range from the fortieth to the sixtieth percentile, lines indicate medians. d, temporal change of annual mean *vpd* by biome. Shown are deviations in percent of the long-term (1980-2018) annual mean. Red (A) represents the polar and subpolar zone; yellow (B) represents the boreal zone; blue (C) represents dry midlatitudes; green (D) represents temperate midlatitudes; purple (E) represents subtropics with year-round rain; orange (F) represents subtropics with winter rain; brown (G) represents dry tropics and subtropics; pink (H) represents tropics with summer rain; and grey (I) represents tropics with year-round rain. e, an exemplary high-resolution map of the climatological mean of *vpd* for the northeastern boundary region of the Andes. For exact location see inset in panel (a).

Surface downwelling shortwave radiation (*rsds*) was highest in the subtropics and tropics, for example northern Africa and the Arabian Peninsula, and decreased towards higher latitudes (Figure 10a). The seasonal variation in *rsds* showed approximately opposite patterns, with lowest seasonal variations in the topics, and highest variations in Antarctica and Greenland (Figure 10b). In terms of northern-hemisphere biomes, *rsds* was lowest in the polar and subpolar zone, from November to January, and highest in the dry tropics and subtropics, especially around June (Figure 10c). Over the past forty years, annual mean *rsds* showed variable trends across northern-hemisphere biomes: in several biomes, for example in the tropics with year-round rain and in particular in the subtropics with year-round rain, *rsds* tended to increase (Figure 10d) whereas in the polar and subpolar zone *rsds* tended to decrease. In the northeastern boundary region of the Andes *rsds* tended to be highest on the Andean plateau and high-elevation mountain peaks and lowest on the northern edge of the Andes on the western slopes on the western edge of the Andes (Figure 10e).
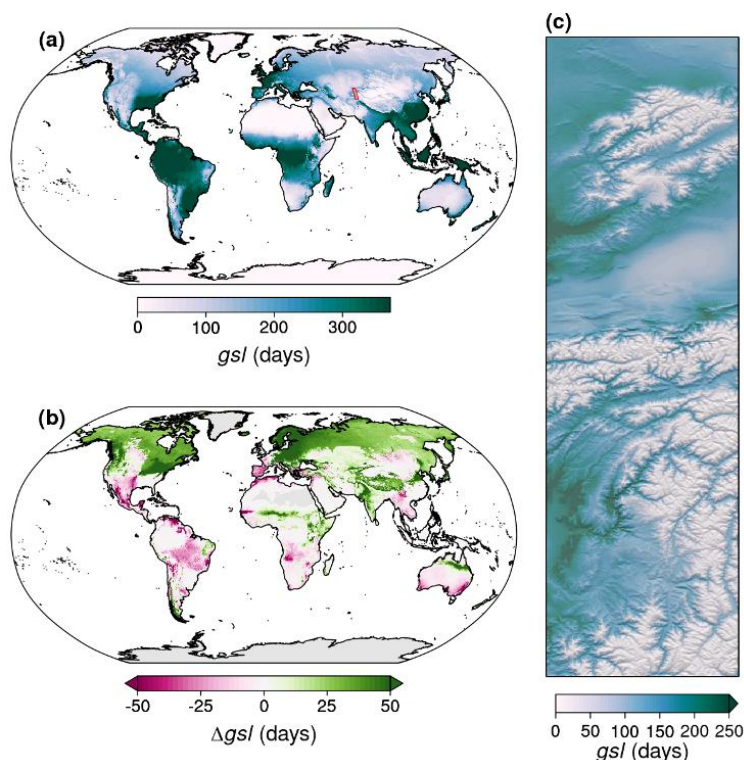
Figure 10: Overview over the spatiotemporal distribution of surface downwelling shortwave (*rsds*): a, global map of the climatological mean for the period 1981-2010; b, global map of the range (max - min) of monthly *rsds* means for the period 1981-2010; c, seasonal cycle of *rsds* in the biomes of the northern hemisphere for the period 1981-2010. Polygons indicate the range from the fortieth to the sixtieth percentile, lines indicate medians. d, temporal change of annual mean *rsds* by biome. Shown are deviations in percent of the long-term (1979-2019) annual mean. Red (A) represents the polar and subpolar zone; yellow (B) represents the boreal zone; blue (C) represents dry midlatitudes; green (D) represents temperate midlatitudes; purple (E) represents subtropics with year-round rain; orange (F) represents subtropics with winter rain; brown (G) represents dry tropics and subtropics; pink (H) represents tropics with summer rain; and grey (I) represents tropics with year-round rain. e, an exemplary high-resolution map of the climatological mean of *rsds* for the northeastern boundary region of the Andes. For exact location see inset in panel (a).

3.1.3 Third-order climate layers

Growing season length (*gsl*) was highest in the tropics, where it typically covered the entire year, and lowest in polar areas, in particular in Greenland and Antarctica, in arid areas, e.g., northern Africa, and in high mountain systems such as the Himalayas, the Rockies or the high Andes (Figure 11a). In the western Himalayas *gsl* was negatively associated with elevation (Figure 11b). Until 2071-2100 *gsl* is expected to increase across most of the temperate-to-high latitudes of the northern hemisphere and in the greater Himalaya region, but also in parts of northern Australia and central-to-eastern Africa, such as Kenya and Ethiopia. Declining growing season lengths are expected for Mexico and the southwestern US, across much of tropical South America, Spain, Morocco, and southern Australia (Figure 11c).

Figure 11: Overview over the spatiotemporal distribution of growing season length (*gsl*): a, global map of the climatological mean of *gsl* for the period 1981-2010; b, global map of the difference between climatological means of 2071-2100 and 1981-2010, assuming anthropogenic emissions to follow the shared socio-economic pathway SSP370 and building on projections of the Max Planck Institute Earth System Model (MPI-ESM 1-2-HR); c, an exemplary high-resolution map of the climatological mean for the western edge of the Himalayas. For exact location see inset in panel (a).

Growing season precipitation (*gsp*) was highest in the tropics and in the Monsoon region of Southern China, and comparably low in desert regions around the globe and in the higher latitudes, except for some coastal areas such as western North America (Figure 12a). Until 2071-2100 *gsp* is expected to increase along the coasts of western and eastern North America, across most of Eurasia, in Oceania and in northern Australia. Decreases are expected in particular in central and tropical America in the Mediterranean region, in western Africa, and in southern Australia (Figure 12b). In the northeastern boundary region of the Andes, *gsp* was highest in the northern lowlands of the Amazon Basin and in particular at the northern edge of the Andes, while it was lowest on the Andean Plateau (Figure 12c).
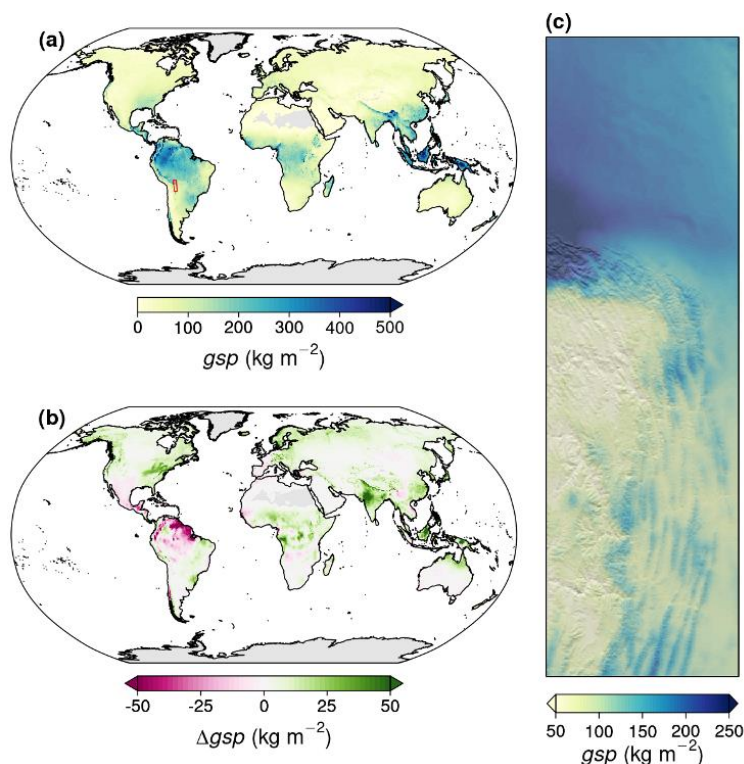
Figure 12: Overview over the spatiotemporal distribution of growing season precipitation (*gsp*): a, global map of the climatological mean of *gsp* for the period 1981-2010; b, global map of the difference between climatological means of 2071-2100 and 1981-2010, assuming anthropogenic emissions to follow the shared socio-economic pathway SSP370 and building on projections of the Max Planck Institute Earth System Model (MPI-ESM 1-2-HR); c, an exemplary high-resolution map of the climatological mean for the northeastern boundary region of the Andes. For exact location see inset in panel (a).

Growing season temperature (*gst*) was highest in the tropics and subtropics and decreased towards the high latitudes (Figure 13a). Until 2071-2100 *gst* is expected to increase in almost all regions of the world with growing seasons, with steepest increases for example in Mauritania. Decreasing growing season temperatures are expected, for example, from southern Sweden, over southern Ukraine to Kazakhstan (Figure 13b). In the northeastern boundary region of the Andes, *gst* was highest in the lowlands and in some inner-alpine valleys, while it was lowest on high-elevation mountain peaks and on the Andean Plateau (Figure 13c).
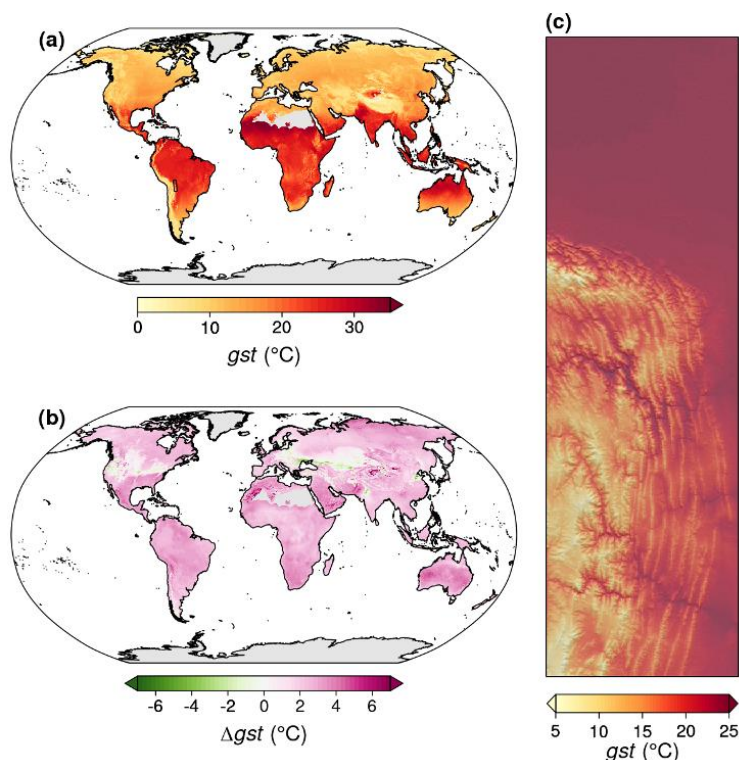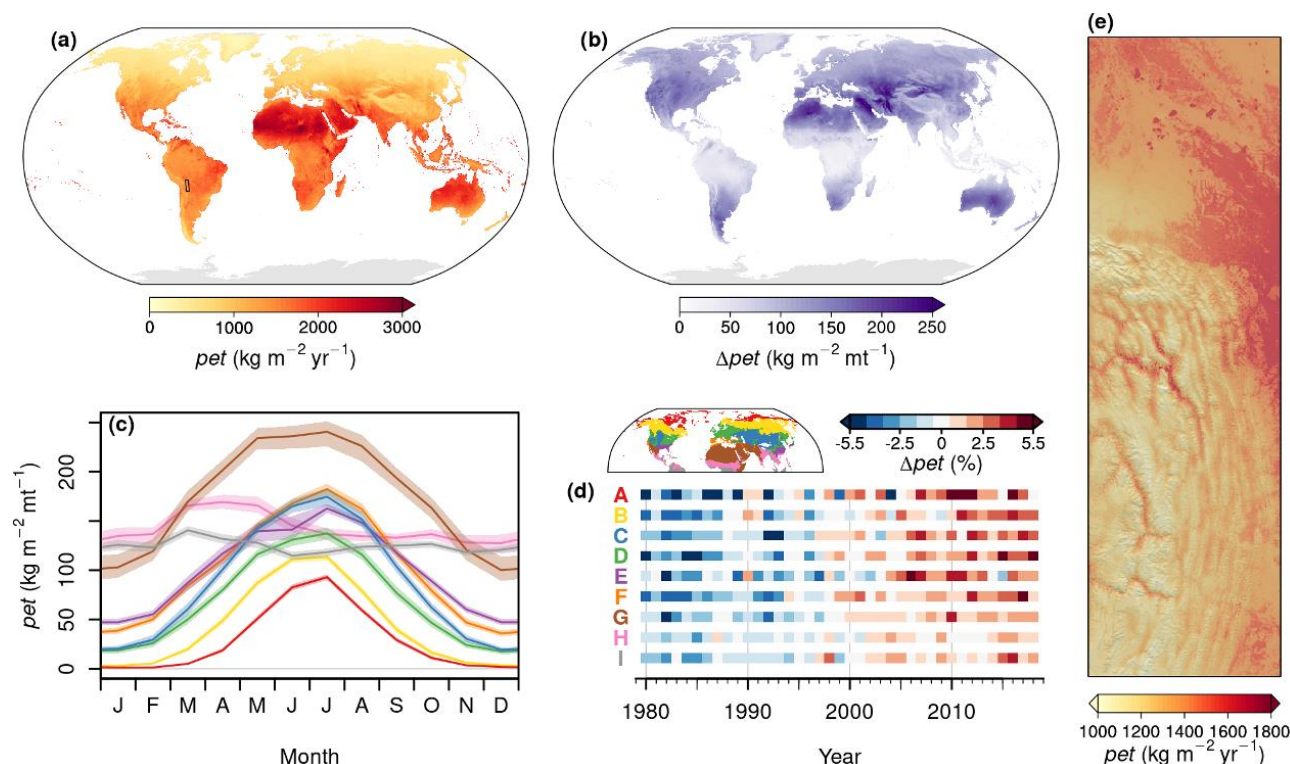
Figure 13: Overview over the spatiotemporal distribution of growing season temperature (*gst*): a, global map of the climatological mean of *gst* for the period 1981-2010; b, global map of the difference between climatological means of 2071-2100 and 1981-2010, assuming anthropogenic emissions to follow the shared socio-economic pathway SSP370 and building on projections of the Max Planck Institute Earth System Model (MPI-ESM 1-2-HR); c, an exemplary high-resolution map of the climatological mean for the northeastern boundary region of the Andes. For exact location see inset in panel (a).

Potential evapotranspiration (*pet*) was highest in the subtropics, such as northern Africa, and decreased towards higher latitudes, and - to a lesser extent - towards the tropics (Figure 14a). The seasonal variation of *pet* was also highest in the subtropics, but its minimum was in the tropics, and in the polar region it was intermediate (Figure 14b). In terms of northern-hemisphere biomes, *pet* was lowest in the polar and subpolar zone, from December to February, and highest in the dry tropics and subtropics, especially from May to July (Figure 14c). Over the past forty years, an increasing trend of annual mean *pet* was observed in all northern-hemisphere biomes (Figure 14d). In the northeastern boundary region of the Andes *pet* showed negative association with elevation, with lowest *pet* on high-elevation mountain peaks and on the Andean plateau and highest values in some inner alpine valleys and in the mideastern lowlands around the city of Santa Cruz. However, *pet* was also relatively low in the lowlands at the northern edge of the Andes, where *clt* and *hurs* were high and *sfcWind* and *rsds* were low (Figure 14e).
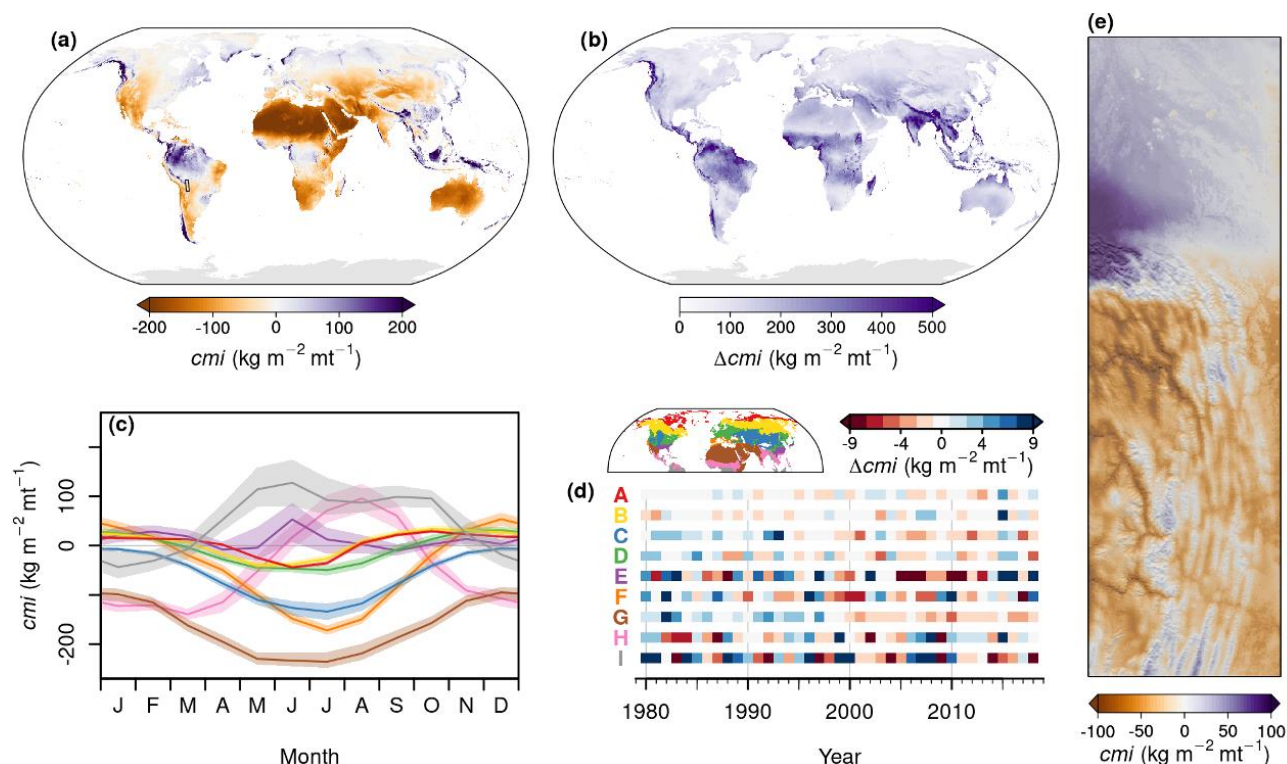
Figure 14: Overview over the spatiotemporal distribution of potential evapotranspiration (*pet*): a, global map of the climatological mean for the period 1981-2010; b, global map of the range (max - min) of monthly *pet* means for the period 1981-2010; c, seasonal cycle of *pet* in the biomes of the northern hemisphere for the period 1981-2010. Polygons indicate the range from the fortieth to the sixtieth percentile, lines indicate medians. d, temporal change of annual mean *pet* by biome. Shown are deviations in percent of the long-term (1980-2018) annual mean. Red (A) represents the polar and subpolar zone; yellow (B) represents the boreal zone; blue (C) represents dry midlatitudes; green (D) represents temperate midlatitudes; purple (E) represents subtropics with year-round rain; orange (F) represents subtropics with winter rain; brown (G) represents dry tropics and subtropics; pink (H) represents tropics with summer rain; and grey (I) represents tropics with year-round rain. e, an exemplary high-resolution map of the climatological mean of *pet* for the northeastern boundary region of the Andes. For exact location see inset in panel (a).

3.1.4 Fourth-order climate layers

Climate moisture index (*cmi*) was highest in parts of the tropics and in some mountain systems, especially in those located close to the coasts, and lowest in northern Africa and the Arabian Peninsula (Figure 15a). The seasonal variation in *cmi* was highest in the tropics and subtropics and in some coastal mountain systems such as the Pacific Northwest of North America, while in high-latitude lowlands variation was comparably low (Figure 15b). In terms of northern-hemisphere biomes, *cmi* was lowest in the dry tropics and subtropics, from May to July, and highest in the tropics with year-round rain, especially in May and June (Figure 15c). Over the past forty years, substantial variations in annual mean *cmi* were observed in northern-hemisphere biomes, mostly without clear temporal trends (Figure 15d). However, *cmi* did show a tendency to decrease in the dry tropics and subtropics. In the northeastern boundary region of the Andes *cmi* was mostly negative, in particular in inner alpine valleys, although at the northern edge of the Andes and in the lowlands of the Amazon basin *cmi* was mostly positive (Figure 15e).
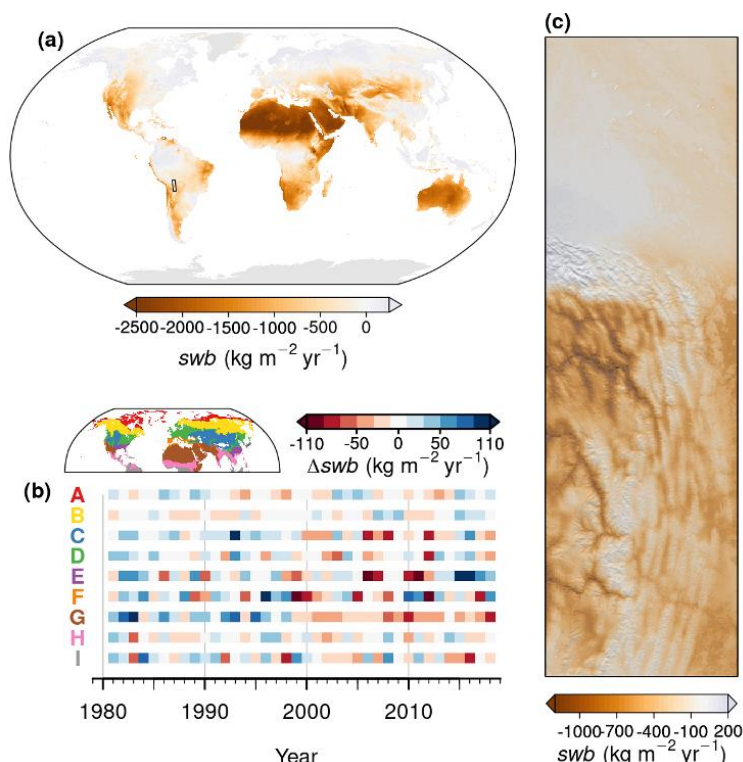
Figure 15: Overview over the spatiotemporal distribution of climate moisture index (*cmi*): a, global map of the climatological mean for the period 1981-2010; b, global map of the range (max-min) of monthly *cmi* means for the period 1981-2010; c, seasonal cycle of *cmi* in the biomes of the northern hemisphere for the period 1981-2010. Polygons indicate the range from the fortieth to the sixtieth percentile, lines indicate medians. d, temporal change of annual mean *cmi* by biome. Shown are deviations in percent of the long-term (1980-2018) annual mean. Red (A) represents the polar and subpolar zone; yellow (B) represents the boreal zone; blue (C) represents dry midlatitudes; green (D) represents temperate midlatitudes; purple (E) represents subtropics with winter rain; orange (F) represents subtropics with year-round rain; brown (G) represents dry tropics and subtropics; pink (H) represents tropics with summer rain; and grey (I) represents tropics with year-round rain. e, an exemplary high-resolution map of the climatological mean of *cmi* for the northeastern boundary region of the Andes. For exact location see inset in panel (a).

3.1.5 Fifth-order climate layers

Site water balance (*swb*) was typically neutral to positive in the tropics and in temperate-to-high latitudes while it was mostly negative elsewhere, most distinctly so in northern Africa and the Arabian Peninsula (Figure 16a). Over the past forty years, substantial variations in annual mean *swb* were observed in northern-hemisphere biomes, mostly without clear temporal trends (Figure 16b). However, *swb* did show a tendency to decrease in the dry tropics and subtropics. In the northeastern boundary region of the Andes and the surrounding lowlands, *swb* was mostly negative, in particular in inner alpine valleys, while it was slightly positive close to the northern edge of the Andes (Figure 16c).

Figure 16: Overview over the spatiotemporal distribution of site water balance (*swb*): a, global map of the climatological mean of
710   *swb* for the period 1981-2010; b, temporal change of annual mean *swb* by biome. Shown are deviations in percent of the long-term
(1980-2018) annual mean. Red (A) represents the polar and subpolar zone; yellow (B) represents the boreal zone; blue (C) represents
dry midlatitudes; green (D) represents temperate midlatitudes; purple (E) represents subtropics with winter rain; orange (F)
represents subtropics with year-round rain; brown (G) represents dry tropics and subtropics; pink (H) represents tropics with
summer rain; and grey (I) represents tropics with year-round rain. c, an exemplary high-resolution map of the climatological mean
715   of *swb* for the northeastern boundary region of the Andes. For exact location see inset in panel (a).

3.2. Validation

The time-series variables we generated showed a good fit with the validation data, especially in the case of *scd*, *gdd₅*, *vpd*, and

pet. The agreement was somewhat lower for *hurs, clt* and *fcf,* and lowest *for sfcWind*. Pearson correlation coefficients (*r*) were

high (*r*>0.85) for *scd, gdd₅, vpd,* and *pet,* for which we also found comparably low MAEs (35.34 days, 1350.9 days °C, 323.6

720   Pa, and 21.80 kg m^{-2} mt^{-1}, respectively). However, with a bias of -30.41 days measured *scd* were notably fewer than our gridded

estimates. For *hurs*, *clt*, and *fcf*, our estimates also correlated reasonably well (*r*>0.80) with the observations and showed

moderately low MAEs of 13.08 %, 22.56 %, and 24.09 days, respectively. For *sfcWind*, correlations were lowest, yet still

acceptable, with an *r* of 0.65 and an MAE of 0.73 m s^{-1}.

Table 1: Validation results for eight climate variables. *r* represents Pearson correlation coefficient; MAE stands for mean absolute
725   error; RMSE stands for root mean squared error; Mean indicates the validation-data averages across all stations considered; Bias
represents the difference between averages of our gridded estimates at station locations and Mean

Variable	Order	Type	Unit	Validation data	*r*	MAE	RMSE	Mean	Bias	# stations

hurs	1	time series	%	FAOCLIM	0.83	13.08	14.48	73.08	-11.90	3109
clt	1	time series	%	GHCN-D	0.84	22.56	23.31	58.21	22.250	250
sfcWind	1	time series	m s^{-1}	GHCN-D	0.65	0.73	0.958	3.41	-0.055	1053
fcf	2	projected	days yr^{-1}	GHCN-D	0.81	24.09	31.46	75.49	7.74	18571
scd	2	projected	days yr^{-1}	GHCN-D	0.90	35.34	48.84	55.79	-30.41	15037
gdd$_5$	2	projected	days °C	GHCN-D	0.96	1350.9	1570	4360.20	1350.2	6700
vpd	2	time series	Pa	FAOCLIM	0.88	323.6	383.4	286.0	683.1	3023
pet	3	time series	kg m^{-2} mt^{-1}	FAOCLIM	0.87	21.80	27.03	120.8	6.182	4246

4 Discussion

Climate data at high spatiotemporal resolution for current conditions and for the decades ahead of us are crucial to fill the gaps
730 in our understanding of climate-change impacts on the Earth system. Here, we provide a dataset of biologically meaningful,
essential climate and environmental variables, combining state-of-the-art input data with a mechanistic downscaling
methodology. The provided gridded layers offer unprecedented spatiotemporal resolution and accuracy. Moreover, they are
comparably robust to gaps in the network of meteorological field stations and therefore provide more reliable estimates in
remote areas, compared to alternatives from station-based interpolations. The comprehensive characterization of climate
735 beyond temperature and precipitation, which includes the computation of water availability, is particularly relevant to study
biological processes (Bojinski et al., 2014; Woodward, 1987; Neilson, 1995). Together, the high spatial and temporal resolution
of our open-access dataset CHELSA-BIOCLIM+ will stimulate research on climate-change impact on physical and ecological
processes.

Comprehensive information on climate beyond temperature and precipitation enables better characterisation of various Earth
740 system processes, and biological processes in particular, where the balance between water supply and energy demand is central
(Woodward, 1987). Our time-series variables related to water availability (*hurs*, *vpd*, *pet*) and incoming solar energy (*clt*, *rsds*,
Karger et al. in prep.) matched particularly well with validation data, and can thus provide valuable inputs to a variety of
downstream analyses such as analysing the distribution of leaf area (Grier and Running, 1977), net primary productivity
(Gholz, 1982) or of plant functional type-based biomes (Neilson, 1995). The biases between downscaled and station-based
745 measurements (lower *hurs*, higher *vpd* and *pet*, Table 1) were generally low, and may to a large part be explained by the
temporal mismatch between the periods covered by the downscaled climatologies (1981-2010) the validation data (1961-
1990). Indeed, all of these variables showed consistent temporal trends in all northern hemisphere biomes over the past forty
years in the same directions as the identified biases (Figures 2, 9, and 14). For *cmi* and *swb*, suitable data for direct validation
are scarce. However, given that the primary additional factor that went into the calculation of these variables, downscaled
750 precipitation, shows a high performance as well (Karger et al., 2020), we can expect that the performance of these two variables
is comparable to the input variables they were computed from. *rsds* was not validated here, but Karger et al. (in prep)
demonstrated that on a daily basis, global *rsds* estimates matched very well with *in situ* measurements (*r*=0.89). A key strength
of the CHELSA-BIOCLIM+ product therefore lies in the provision of accurate, high-resolution, global time-series of climate-
related variables describing the true availability of water and solar energy.

755 Combining input data from reanalysis with mechanistic downscaling approaches allows for robust estimates in particular in
remote areas. So far, climate data used in macroecological analyses often relied on station-based interpolations (e.g., Hijmans
et al., 2005). While such data may be accurate in regions that have a dense network of field stations, they are much less reliable
in remote areas, and/or in complex terrain (Karger et al., 2017). The CHELSA approach, on the other hand, uses interpolations
between stations that account for physical mesoscale atmospheric processes (Hersbach et al., 2020) and further accounts for
760 major orographic effects such as the shading of terrain or wind exposure (e.g., for *hurs*, *clt*, and *pet*, see methods). Given the

lack of field stations in remote areas, the extent of these improvements is likely not fully mirrored in the validation results. However, their relevance is illustrated by the realistic patterns in our exemplary remote-area, high-resolution maps in Figures 2-16, suggesting that the CHELSA-BIOCLIM+ product offers improved data particularly in remote areas.

765 Generating a comprehensive global set of high-resolution climate-related variables requires making generalising assumptions that can compromise the accuracy of some estimates. This was especially the case for our projected variables that provide current and future estimates. As highlighted by the validation, our estimates of *scd* overestimated station-based measurements by about one month in regions with snow. These differences may arise from generating estimates of daily *tas*, *tasmin*, *tasmax*, and *pr* from monthly averages by means of spline interpolation, which results in a more gradual seasonal evolution of temperature and precipitation than observed in natural weather patterns. Moreover, for *scd*, important factors such as solar

770 radiation were ignored and the model to generate estimates for *gsl*, *gsp*, and *gst* contained a simplistic implementation of soil water processes. However, the approaches used to generate projected variables were not primarily selected for their accuracy, but for their generalism (Levins, 1966) to be applicable under current *and* projected future conditions and to avoid overfitting. Despite significant advances during the past years (Kawamiya et al., 2020) Earth system models are still not capable of fully resolving mesoscale weather processes and thus they are primarily suited to study long-term changes in climate rather than

775 possible weather patterns (Held et al., 2019; Yukimoto et al., 2019; Gutjahr et al., 2019; Boucher et al., 2020). Relative to our time-series variables, our projected variables may therefore not offer the same high accuracy for the recent past, but they approximate biologically and ecologically meaningful quantities that are directly comparable between current and a variety of possible future conditions, and build on the most accurate global prognoses that are currently available (Eyring et al., 2016). The validation also revealed inaccuracies for the time-series variable *sfcWind*. The limited accuracy of *sfcWind* may result

780 from the simpler delta-change-type downscaling method employed, compared to the other time-series variables. Alternatively, it may originate from the inherently high variance of this variable, for which even the most sophisticated downscaling approaches yield limited accuracy (Pryor and Hahmann, 2019).

In conclusion, CHELSA-BIOCLIM+ is a comprehensive spatial and temporal data set of 15 climate-related variables including both, time-series for the past forty years and future projections building on several SSPs and Earth system models. Besides the

785 climatological statistics provided, these data may be used to compute additional summaries, for example interannual variabilities of *cmi*, which are important factors determining ecosystem structure in the dry midlatitudes, subtropics and tropics (Schultz, 2005). Moreover, the downscaling pipeline developed here opens new perspectives to develop near real-time risk assessments when regularly updated and combined with machine learning and increasingly available global phenomenological datasets. The higher temporal resolution and the more proximal variables included in the CHELSA-BIOCLIM+ product will

790 allow for a more detailed characterization of climate-related conditions and, in turn, a deeper understanding of their impact on key environmental processes.

Data availability

The CHELSA-BIOCLIM+ data set consists of 4006 single-layer GeoTIFF files, representing averages, extrema, and ranges of
795 the 15 climate-related variables for different time points (1979 to 2100) and periods (monthly to 30-year-averages). The
GeoTIFF files are stored on a S3 cloud server that can be accessed over EnviDat (https://doi.org/10.16904/envidat.332; Brun
et al., 2022), by clicking on the 'CHELSA-BIOCLIM+' box in the 'Data and resources' tab, and over www.chelsa-climate.org,
by clicking on 'Version 2.1' under 'Downloads'. This file browser contains the four folders 'annual', 'daily', 'monthly', and
'climatologies' within which the CHELSA-BIOCLIM+ data are organized in the following way:

800 • The folder 'annual' contains the subfolder 'swb', which contains annual layers of *swb*.

• The folder 'daily' contains no data of the CHELSA-BIOCLIM+ data set.

• The folder 'monthly' contains (among folders from other data sets) the subfolders 'clt', 'cmi', 'hurs', 'pet', 'rsds', 'sfcWind', and 'vpd' which contain monthly layers for *clt*, *cmi*, *hurs*, *pet*, *rsds*, *sfcWind*, and *vpd*, respectively.

• The folder 'climatologies' contains four subfolders, '1981-2010', '2011-2040', '2041-2070', and '2071-2100', that
805 represent the different time periods for which climatologies are representative.

    o In the subfolder '1981-2010' the sub-subfolders 'clt', 'cmi', 'hurs', 'pet', 'rsds', 'sfcWind', and 'vpd' contain 1981-2010 averages of *clt*, *cmi*, *hurs*, *pet*, *rsds*, *sfcWind*, and *vpd*, respectively, for each month. The sub-subfolder 'bio' contains (among files from other data sets) climatological means, maxima, minima and annual ranges for *clt*, *cmi*, *hurs*, *pet*, *rsds*, *sfcWind*, and *vpd*, and climatological means for *fcf*, *gdd* (with 0
810 °C, 5 °C, and 10 °C baseline temperature, i.e., 'gdd0', 'gdd5', 'gdd10', respectively), *gsl*, *gsp*, *gst*, *npp*, *scd*, and *swb*.

    o The subfolders '2010-2040', '2041-2070', and '2071-2100' each contain one sub-subfolder per Earth system model considered (i.e., the sub-subfolders 'GFDL-ESM4', 'IPSL-CM6A-LR', 'MPI-ESM1-2-HR', 'MRI-ESM2-0', 'UKESM1-0-LL'). Each of these combinations between period and Earth system model contains
815 three sub-sub-subfolders representing the three SSPs (i.e., the sub-sub-subfolders 'ssp126', 'ssp370', and 'ssp585'); and each of these combinations between period, Earth system model, and SSP, contains a sub-sub-sub-subfolder 'bio' that contains (among files from other data sets) climatological means for *fcf*, *gdd* (with 0 °C, 5 °C, and 10 °C baseline temperature), *gsl*, *gsp*, *gst*, *npp*, and *scd*.

More information on naming and settings of the GeoTIFF files (grid structure, unit, scale and offset parameters) can be
820 found in the subsection '2.4 Output format and file organization' and in the Technical Documentation PDF that can be found on https://doi.org/10.16904/envidat.332 in the 'CHELSA-BIOCLIM+ Technical Documentation' box in the 'Data and resources' tab. Monthly and annual layers of the time-series variables will occasionally be added to the CHELSA-BIOCLIM+ data set, to extend the time period covered to the most recent years.

825

Author contribution

PB, DNK, NEZ, and LP conceived the general idea of the paper. PB and DNK generated the data set. CH conducted the validation with support of PB and DNK. PB led the writing of the manuscript. All authors significantly contributed to writing and editing.

Competing interests

The authors declare that they have no conflict of interest.

Earth System

Science

Data

Open Access

Discussions

References

Allen, R. G., Pereira, L. S., Raes, D., and Smith, M.: Crop evapotranspiration —guidelines for computing crop water requirements, FAO Irrig. Drain. Pap., 56, 1998.

Anandhi, A.: Growing degree days – Ecosystem indicator for changing diurnal temperatures and their impact on corn growth 845   stages in Kansas, Ecol. Indic., 61, 149–158, https://doi.org/10.1016/j.ecolind.2015.08.023, 2016.

Andrade, A. M. De, Michel, R. F. M., Bremer, U. F., Schaefer, C. E. G. R., and Simões, J. C.: Relationship between solar radiation and surface distribution of vegetation in Fildes Peninsula and Ardley Island, Maritime Antarctica, Int. J. Remote Sens., 39, 2238–2254, https://doi.org/10.1080/01431161.2017.1420937, 2018.

Araújo, M. B. and Rahbek, C.: How Does Climate Change Affect Biodiversity?, Science (80-.)., 313, 1396–1397, 850   https://doi.org/10.1126/science.1131758, 2006.

Arguez, A. and Vose, R. S.: The Definition of the Standard WMO Climate Normal: The Key to Deriving Alternative Climate Normals, Bull. Am. Meteorol. Soc., 92, 699–704, https://doi.org/10.1175/2010BAMS2955.1, 2011.

Bellard, C., Bertelsmeier, C., Leadley, P., Thuiller, W., and Courchamp, F.: Impacts of climate change on the future of biodiversity, Ecol. Lett., 15, 365–377, https://doi.org/10.1111/j.1461-0248.2011.01736.x, 2012.

855   Böhner, J. and Antonic, O.: Land-Surface Parameters Specific to Topo-Climatology, in: GEOMORPHOMETRY: CONCEPTS, SOFTWARE, APPLICATIONS, 195–226, https://doi.org/10.1016/S0166-2481(08)00008-1, 2009.

Bojinski, S., Verstraete, M., Peterson, T. C., Richter, C., Simmons, A., and Zemp, M.: The Concept of Essential Climate Variables in Support of Climate Research, Applications, and Policy, Bull. Am. Meteorol. Soc., 95, 1431–1443, https://doi.org/10.1175/BAMS-D-13-00047.1, 2014.

860   Boucher, O., Servonnat, J., Albright, A. L., Aumont, O., Balkanski, Y., Bastrikov, V., Bekki, S., Bonnet, R., Bony, S., Bopp, L., Braconnot, P., Brockmann, P., Cadule, P., Caubel, A., Cheruy, F., Codron, F., Cozic, A., Cugnet, D., D'Andrea, F., Davini, P., Lavergne, C., Denvil, S., Deshayes, J., Devilliers, M., Ducharne, A., Dufresne, J., Dupont, E., Éthé, C., Fairhead, L., Falletti, L., Flavoni, S., Foujols, M., Gardoll, S., Gastineau, G., Ghattas, J., Grandpeix, J., Guenet, B., Guez, Lionel, E., Guilyardi, E., Guimberteau, M., Hauglustaine, D., Hourdin, F., Idelkadi, A., Joussaume, S., Kageyama, M., Khodri, M., Krinner, G., Lebas, 865   N., Levavasseur, G., Lévy, C., Li, L., Lott, F., Lurton, T., Luyssaert, S., Madec, G., Madeleine, J., Maignan, F., Marchand, M., Marti, O., Mellul, L., Meurdesoif, Y., Mignot, J., Musat, I., Ottlé, C., Peylin, P., Planton, Y., Polcher, J., Rio, C., Rochetin, N., Rousset, C., Sepulchre, P., Sima, A., Swingedouw, D., Thiéblemont, R., Traore, A. K., Vancoppenolle, M., Vial, J., Vialard, J., Viovy, N., and Vuichard, N.: Presentation and Evaluation of the IPSL-CM6A-LR Climate Model, J. Adv. Model. Earth Syst., 12, https://doi.org/10.1029/2019MS002010, 2020.

870   Brun, P., Zimmermann, N. E., Hari, C., Pellissier, L., and Karger, D. N.: CHELSA-BIOCLIM+ A novel set of global climate-related predictors at kilometre-resolution, https://doi.org/10.16904/envidat.332, 2022.

Callaghan, T. V., Johansson, M., Brown, R. D., Groisman, P. Y., Labba, N., Radionov, V., Bradley, R. S., Blangy, S., Bulygina, O. N., Christensen, T. R., Colman, J. E., Essery, R. L. H., Forbes, B. C., Forchhammer, M. C., Golubev, V. N., Honrath, R.

E., Juday, G. P., Meshcherskaya, A. V., Phoenix, G. K., Pomeroy, J., Rautio, A., Robinson, D. A., Schmidt, N. M., Serreze,

875 M. C., Shevchenko, V. P., Shiklomanov, A. I., Shmakin, A. B., Sköld, P., Sturm, M., Woo, M., and Wood, E. F.: Multiple

Effects of Changes in Arctic Snow Cover, Ambio, 40, 32–45, https://doi.org/10.1007/s13280-011-0213-x, 2011.

Cayton, H. L., Haddad, N. M., Gross, K., Diamond, S. E., and Ries, L.: Do growing degree days predict phenology across

butterfly species?, Ecology, 96, 1473–1479, https://doi.org/10.1890/15-0131.1, 2015.

Conrad, O., Bechtel, B., Bock, M., Dietrich, H., Fischer, E., Gerlitz, L., Wehberg, J., Wichmann, V., and Böhner, J.: System

880 for Automated Geoscientific Analyses (SAGA) v. 2.1.4, Geosci. Model Dev., 8, 1991–2007, https://doi.org/10.5194/gmd-8-

1991-2015, 2015.

Danielson, J. J. and Gesch, D. B.: Global multi-resolution terrain elevation data 2010 (GMTED2010),

https://doi.org/10.5066/F7J38R2N, 2011.

Dawson, T. E.: Fog in the California redwood forest: ecosystem inputs and use by plants, Oecologia, 117, 476–485,

885 https://doi.org/10.1007/s004420050683, 1998.

Easterling, D. R., Meehl, G. A., Parmesan, C., Changnon, S. A., Karl, T. R., and Mearns, L. O.: Climate Extremes:

Observations, Modeling, and Impacts, Science (80-.)., 289, 2068–2074, https://doi.org/10.1126/science.289.5487.2068, 2000.

Easterling, D. R., Kunkel, K. E., Wehner, M. F., and Sun, L.: Detection and attribution of climate extremes in the observed

record, Weather Clim. Extrem., 11, 17–27, https://doi.org/10.1016/j.wace.2016.01.001, 2016.

890 Elsen, P. R., Monahan, W. B., Dougherty, E. R., and Merenlender, A. M.: Keeping pace with climate change in global

terrestrial protected areas, Sci. Adv., 6, https://doi.org/10.1126/sciadv.aay0814, 2020.

Evans, B. M., Walker, D. A., Benson, C. S., Nordstrand, E. A., and Petersen, G. W.: Spatial interrelationships between terrain,

snow distribution and vegetation patterns at an arctic foothills site in Alaska, Ecography (Cop.)., 12, 270–278,

https://doi.org/10.1111/j.1600-0587.1989.tb00846.x, 1989.

895 Eyring, V., Bony, S., Meehl, G. A., Senior, C. A., Stevens, B., Stouffer, R. J., and Taylor, K. E.: Overview of the Coupled

Model Intercomparison Project Phase 6 (CMIP6) experimental design and organization, Geosci. Model Dev., 9, 1937–1958,

https://doi.org/10.5194/gmd-9-1937-2016, 2016.

FAO: FAOCLIM 2: world-wide agroclimatic data, 2001.

Gholz, H. L.: Environmental Limits on Aboveground Net Primary Production, Leaf Area, and Biomass in Vegetation Zones

900 of the Pacific Northwest, Ecology, 63, 469–481, https://doi.org/10.2307/1938964, 1982.

Grier, C. G. and Running, S. W.: Leaf Area of Mature Northwestern Coniferous Forests: Relation to Site Water Balance,

Ecology, 58, 893–899, https://doi.org/10.2307/1936225, 1977.

Grossiord, C., Buckley, T. N., Cernusak, L. A., Novick, K. A., Poulter, B., Siegwolf, R. T. W., Sperry, J. S., and McDowell,

N. G.: Plant responses to rising vapor pressure deficit, New Phytol., 226, 1550–1566, https://doi.org/10.1111/nph.16485, 2020.

905 Gutjahr, O., Putrasahan, D., Lohmann, K., Jungclaus, J. H., von Storch, J.-S., Brüggemann, N., Haak, H., and Stössel, A.: Max

Planck Institute Earth System Model (MPI-ESM1.2) for the High-Resolution Model Intercomparison Project (HighResMIP),

Geosci. Model Dev., 12, 3241–3281, https://doi.org/10.5194/gmd-12-3241-2019, 2019.

Hannah, L.: Protected Areas and Climate Change, Ann. N. Y. Acad. Sci., 1134, 201–212, https://doi.org/10.1196/annals.1439.009, 2008.

910 Hargreaves, G. H. and Samani, Z. A.: Reference Crop Evapotranspiration from Temperature, Appl. Eng. Agric., 1, 96–99, https://doi.org/10.13031/2013.26773, 1985.

Hartman, M. D., Parton, W. J., Derner, J. D., Schulte, D. K., Smith, W. K., Peck, D. E., Day, K. A., Del Grosso, S. J., Lutz, S., Fuchs, B. A., Chen, M., and Gao, W.: Seasonal grassland productivity forecast for the U.S. Great Plains using Grass-Cast, 11, https://doi.org/10.1002/ecs2.3280, 2020.

915 Hauser, G., Rais, O., Morán Cadenas, F., Gonseth, Y., Bouzelboudjen, M., and Gern, L.: Influence of climatic factors on Ixodes ricinus nymph abundance and phenology over a long-term monthly observation in Switzerland (2000–2014), Parasit. Vectors, 11, 289, https://doi.org/10.1186/s13071-018-2876-7, 2018.

Hay, L. E., Wilby, R. L., and Leavesley, G. H.: A COMPARISON OF DELTA CHANGE AND DOWNSCALED GCM SCENARIOS FOR THREE MOUNTAINOUS BASINS IN THE UNITED STATES 1, JAWRA J. Am. Water Resour. Assoc.,
920 36, 387–397, https://doi.org/10.1111/j.1752-1688.2000.tb04276.x, 2000.

Held, I. M., Guo, H., Adcroft, A., Dunne, J. P., Horowitz, L. W., Krasting, J., Shevliakova, E., Winton, M., Zhao, M., Bushuk, M., Wittenberg, A. T., Wyman, B., Xiang, B., Zhang, R., Anderson, W., Balaji, V., Donner, L., Dunne, K., Durachta, J., Gauthier, P. P. G., Ginoux, P., Golaz, J. -C., Griffies, S. M., Hallberg, R., Harris, L., Harrison, M., Hurlin, W., John, J., Lin, P., Lin, S. -J., Malyshev, S., Menzel, R., Milly, P. C. D., Ming, Y., Naik, V., Paynter, D., Paulot, F., Ramaswamy, V., Reichl,
925 B., Robinson, T., Rosati, A., Seman, C., Silvers, L. G., Underwood, S., and Zadeh, N.: Structure and Performance of GFDL's CM4.0 Climate Model, J. Adv. Model. Earth Syst., 11, 3691–3727, https://doi.org/10.1029/2019MS001829, 2019.

Hengl, T., de Jesus, J. M., MacMillan, R. A., Batjes, N. H., Heuvelink, G. B. M., Ribeiro, E., Samuel-Rosa, A., Kempen, B., Leenaars, J. G. B., Walsh, M. G., and Gonzalez, M. R.: SoilGrids1km — Global Soil Information Based on Automated Mapping, PLoS One, 9, e105992, https://doi.org/10.1371/journal.pone.0105992, 2014.

930 Hengl, T., Mendes de Jesus, J., Heuvelink, G. B. M., Ruiperez Gonzalez, M., Kilibarda, M., Blagotić, A., Shangguan, W., Wright, M. N., Geng, X., Bauer-Marschallinger, B., Guevara, M. A., Vargas, R., MacMillan, R. A., Batjes, N. H., Leenaars, J. G. B., Ribeiro, E., Wheeler, I., Mantel, S., and Kempen, B.: SoilGrids250m: Global gridded soil information based on machine learning, PLoS One, 12, e0169748, https://doi.org/10.1371/journal.pone.0169748, 2017.

Hersbach, H., Bell, B., Berrisford, P., Hirahara, S., Horányi, A., Muñoz-Sabater, J., Nicolas, J., Peubey, C., Radu, R., Schepers,
935 D., Simmons, A., Soci, C., Abdalla, S., Abellan, X., Balsamo, G., Bechtold, P., Biavati, G., Bidlot, J., Bonavita, M., Chiara, G., Dahlgren, P., Dee, D., Diamantakis, M., Dragani, R., Flemming, J., Forbes, R., Fuentes, M., Geer, A., Haimberger, L., Healy, S., Hogan, R. J., Hólm, E., Janisková, M., Keeley, S., Laloyaux, P., Lopez, P., Lupu, C., Radnoti, G., Rosnay, P., Rozum, I., Vamborg, F., Villaume, S., and Thépaut, J.: The ERA5 global reanalysis, Q. J. R. Meteorol. Soc., 146, 1999–2049, https://doi.org/10.1002/qj.3803, 2020.

940 Hijmans, R. J.: raster: Geographic Data Analysis and Modeling, https://cran.r-project.org/package=raster, 2019.

Hijmans, R. J., Cameron, S. E., Parra, J. L., Jones, P. G., and Jarvis, A.: Very high resolution interpolated climate surfaces for

global land areas, Int. J. Climatol., 25, 1965–1978, https://doi.org/10.1002/joc.1276, 2005.

Hogg, E. H.: Temporal scaling of moisture and the forest-grassland boundary in western Canada, Agric. For. Meteorol., 84, 115–122, https://doi.org/10.1016/S0168-1923(96)02380-5, 1997.

945 Hogg, E. H., Michaelian, M., Hook, T. I., and Undershultz, M. E.: Recent climatic drying leads to age-independent growth reductions of white spruce stands in western Canada, Glob. Chang. Biol., 23, 5297–5308, https://doi.org/10.1111/gcb.13795, 2017.

Howden, S. M., Soussana, J.-F., Tubiello, F. N., Chhetri, N., Dunlop, M., and Meinke, H.: Adapting agriculture to climate change, Proc. Natl. Acad. Sci., 104, 19691–19696, https://doi.org/10.1073/pnas.0701890104, 2007.

950 Hufkens, K., Friedl, M. A., Keenan, T. F., Sonnentag, O., Bailey, A., O'Keefe, J., and Richardson, A. D.: Ecological impacts of a widespread frost event following early spring leaf-out, Glob. Chang. Biol., 18, 2365–2377, https://doi.org/10.1111/j.1365-2486.2012.02712.x, 2012.

IPBES: Summary for policymakers of the regional assessment report on biodiversity and ecosystem services for Europe and Central Asia of the Intergovernmental Science-Policy Platform on Biodiversity and Ecosystem Services eds., edited by:
955 Fischer, M., Rounsevell, M., Torre-Marin Rando, A., and Mader, A., Bonn, Germany, 48 pp., 2018.

IPCC: Renewable Energy Sources and Climate Change Mitigation: Special Report of the Intergovernmental Panel on Climate Change, edited by: Edenhofer, O., Pichs-Madruga, R., Sokona, Y., Seyboth, K., Matschoss, P., Kadner, S., Zwickel, T., Eickemeier, P., Hansen, G., Schlömer, S., and von Stechow, C., Cambridge University Press, Cambridge, 2011.

IPCC: Climate Change 2022: Impacts, Adaptation, and Vulnerability. Contribution of Working Group II to the Sixth
960 Assessment Report of the Intergovernmental Panel on Climate Change, edited by: Pörtner, H.-O., Roberts, D. C., Tignor, M., Poloczanska, E. S., Mintenbeck, K., Alegría, A., Craig, M., Langsdorf, S., Löschke, S., Möller, V., Okem, A., and Rama, B., Cambridge University Press, United Kingdom, https://doi.org/https://www.ipcc.ch/report/ar6/wg2/downloads/report/IPCC_AR6_WGII_FinalDraft_Chapter13.pdf, 2022.

Irmak, S.: Evapotranspiration, in: Encyclopedia of Ecology, Elsevier, 1432–1438, https://doi.org/10.1016/B978-008045405-
965 4.00270-6, 2008.

Karger, D. N., Conrad, O., Böhner, J., Kawohl, T., Kreft, H., Soria-Auza, R. W., Zimmermann, N. E., Linder, H. P., and Kessler, M.: Climatologies at high resolution for the earth's land surface areas, Sci. Data, 4, 170122, https://doi.org/10.1038/sdata.2017.122, 2017.

Karger, D. N., Schmatz, D. R., Dettling, G., and Zimmermann, N. E.: High-resolution monthly precipitation and temperature
970 time series from 2006 to 2100, Sci. Data, 7, 248, https://doi.org/10.1038/s41597-020-00587-y, 2020.

Karger, D. N., S., L., Hari, C., Reyer, C. P. O., and Zimmermann, N. E.: CHELSA-W5E5 v1.1: W5E5 v1.0 downscaled with CHELSA v2.0., https://doi.org/10.48364/ISIMIP.836809.1, 2021a.

Karger, D. N., Conrad, O., Böhner, J., Kawohl, T., Kreft, H., Soria-Auza, R. W., Zimmermann, N. E., Linder, H. P., and Kessler, M.: Climatologies at high resolution for the earth's land surface areas, https://doi.org/10.16904/envidat.228.v2.1,
975 2021b.

Karger, D. N., Wilson, A. M., Mahony, C., Zimmermann, N. E., and Jetz, W.: Global daily 1 km land surface precipitation based on cloud cover-informed downscaling, Sci. Data, 8, 307, https://doi.org/10.1038/s41597-021-01084-6, 2021c.

Karger, D. N., Kessler, M., Lehnert, M., and Jetz, W.: Limited protection and ongoing loss of tropical cloud forest biodiversity and ecosystems worldwide, Nat. Ecol. Evol., 5, 854–862, https://doi.org/10.1038/s41559-021-01450-y, 2021d.

980   Karger, D. N., Lange, S., Hari, C., Reyer, C. P. O., Zimmermann, N. E., and Frieler, K.: CHELSA-W5E5 v1.0: daily 1km meteorological forcing data for climate impact studies, Target ESSD, n.d.

Kawamiya, M., Hajima, T., Tachiiri, K., Watanabe, S., and Yokohata, T.: Two decades of Earth system modeling with an emphasis on Model for Interdisciplinary Research on Climate (MIROC), Prog. Earth Planet. Sci., 7, 64, https://doi.org/10.1186/s40645-020-00369-5, 2020.

985   Knauer, J., El-Madany, T. S., Zaehle, S., and Migliavacca, M.: Bigleaf—An R package for the calculation of physical and physiological ecosystem properties from eddy covariance data, PLoS One, 13, e0201114, https://doi.org/10.1371/journal.pone.0201114, 2018.

Körner, C., Paulsen, J., and Spehn, E. M.: A definition of mountains and their bioclimatic belts for global comparisons of biodiversity data, Alp. Bot., 121, 73, https://doi.org/10.1007/s00035-011-0094-4, 2011.

990   Lange, S.: ISIMIP3b bias adjustment fact sheet, 40 pp., 2021.

Larcher, W.: Ökophysiologie der Pflanzen: Leben und Stressbewältigung der Pflanzen in ihrer Umwelt., 5th ed., Verlag Eugen Ulmer, Stuttgart, 394 pp., 1994.

Leng, G. and Hall, J.: Crop yield sensitivity of global major agricultural countries to droughts and the projected changes in the future, Sci. Total Environ., 654, 811–821, https://doi.org/10.1016/j.scitotenv.2018.10.434, 2019.

995   Lenihan, J. M.: Ecological response surfaces for North American boreal tree species and their use in forest classification, J. Veg. Sci., 4, 667–680, https://doi.org/10.2307/3236132, 1993.

Levins, R.: THE STRATEGY OF MODEL BUILDING IN POPULATION BIOLOGY, Am. Sci., 54, 421–431, 1966.

Lieth, H.: Modeling the Primary Productivity of the World, 237–263, https://doi.org/10.1007/978-3-642-80913-2_12, 1975.

Menne, M. J., Durre, I., Vose, R. S., Gleason, B. E., and Houston, T. G.: An Overview of the Global Historical Climatology

1000   Network-Daily Database, J. Atmos. Ocean. Technol., 29, 897–910, https://doi.org/10.1175/JTECH-D-11-00103.1, 2012.

Monteith, J. L.: Evaporation and environment, Symp. Soc. Exp. Biol., 19, 205–234, 1965.

Muñoz-Sabater, J.: ERA5-Land monthly averaged data from 1950 to 1980, https://doi.org/10.24381/cds.68d2bb3, 2021.

Muñoz Sabater, J.: ERA5-Land monthly averaged data from 1981 to present, https://doi.org/10.24381/cds.68d2bb3, 2019.

Neilson, R. P.: A Model for Predicting Continental-Scale Vegetation Distribution and Water Balance, Ecol. Appl., 5, 362–

1005   385, https://doi.org/10.2307/1942028, 1995.

Nemani, R. R., Keeling, C. D., Hashimoto, H., Jolly, W. M., Piper, S. C., Tucker, C. J., Myneni, R. B., and Running, S. W.: Climate-Driven Increases in Global Terrestrial Net Primary Production from 1982 to 1999, Science (80-.)., 300, 1560–1563, https://doi.org/10.1126/science.1082750, 2003.

Nobel, P. S.: Wind as an Ecological Factor, in: Physiological Plant Ecology I, Springer Berlin Heidelberg, Berlin, Heidelberg,

1010 475–500, https://doi.org/10.1007/978-3-642-68090-8_16, 1981.

O'Neill, B. C., Kriegler, E., Riahi, K., Ebi, K. L., Hallegatte, S., Carter, T. R., Mathur, R., and van Vuuren, D. P.: A new scenario framework for climate change research: the concept of shared socioeconomic pathways, Clim. Change, 122, 387–400, https://doi.org/10.1007/s10584-013-0905-2, 2014.

O'Neill, B. C., Tebaldi, C., van Vuuren, D. P., Eyring, V., Friedlingstein, P., Hurtt, G., Knutti, R., Kriegler, E., Lamarque, J.-
1015 F., Lowe, J., Meehl, G. A., Moss, R., Riahi, K., and Sanderson, B. M.: The Scenario Model Intercomparison Project (ScenarioMIP) for CMIP6, Geosci. Model Dev., 9, 3461–3482, https://doi.org/10.5194/gmd-9-3461-2016, 2016.

O'Neill, B. C., Kriegler, E., Ebi, K. L., Kemp-Benedict, E., Riahi, K., Rothman, D. S., van Ruijven, B. J., van Vuuren, D. P., Birkmann, J., Kok, K., Levy, M., and Solecki, W.: The roads ahead: Narratives for shared socioeconomic pathways describing world futures in the 21st century, Glob. Environ. Chang., 42, 169–180, https://doi.org/10.1016/j.gloenvcha.2015.01.004, 2017.

1020 Ooms, J.: magick: Advanced Graphics and Image-Processing in R, https://cran.r-project.org/package=magick, 2020.

Ouisse, T., Bonte, D., Lebouvier, M., Hendrickx, F., and Renault, D.: The importance of relative humidity and trophic resources in governing ecological niche of the invasive carabid beetle Merizodus soledadinus in the Kerguelen archipelago, J. Insect Physiol., 93–94, 42–49, https://doi.org/10.1016/j.jinsphys.2016.08.006, 2016.

Paulsen, J. and Körner, C.: A climate-based model to predict potential treeline position around the globe, Alp. Bot., 124, 1–
1025 12, https://doi.org/10.1007/s00035-014-0124-0, 2014.

Pebesma, E. J. and Bivand, R. S.: Classes and methods for spatial data in {R}, R News, 5, 9–13, 2005.

Pollock, L. J., Thuiller, W., and Jetz, W.: Large conservation gains possible for global biodiversity facets, Nature, 546, 141–144, https://doi.org/10.1038/nature22368, 2017.

Prentice, I. C., Cramer, W., Harrison, S. P., Leemans, R., Monserud, R. A., and Solomon, A. M.: Special Paper: A Global
1030 Biome Model Based on Plant Physiology and Dominance, Soil Properties and Climate, J. Biogeogr., 19, 117, https://doi.org/10.2307/2845499, 1992.

Pryor, S. C. and Hahmann, A. N.: Downscaling Wind, in: Oxford Research Encyclopedia of Climate Science, Oxford University Press, https://doi.org/10.1093/acrefore/9780190228620.013.730, 2019.

R Development Core Team: R: A Language and Environment for Statistical Computing, http://www.r-project.org, 2008.

1035 Santini, M., Noce, S., Antonelli, M., and Caporaso, L.: Complex drought patterns robustly explain global yield loss for major crops, Sci. Rep., 12, 5792, https://doi.org/10.1038/s41598-022-09611-0, 2022.

Schimel, D. S.: Terrestrial ecosystems and the carbon cycle, Glob. Chang. Biol., 1, 77–91, https://doi.org/10.1111/j.1365-2486.1995.tb00008.x, 1995.

Schultz, J.: The Ecozones of the World, Springer Berlin Heidelberg, Berlin, Heidelberg, https://doi.org/10.1007/3-540-28527-
1040 X, 2005.

Sellar, A. A., Jones, C. G., Mulcahy, J. P., Tang, Y., Yool, A., Wiltshire, A., O'Connor, F. M., Stringer, M., Hill, R., Palmieri, J., Woodward, S., Mora, L., Kuhlbrodt, T., Rumbold, S. T., Kelley, D. I., Ellis, R., Johnson, C. E., Walton, J., Abraham, N. L., Andrews, M. B., Andrews, T., Archibald, A. T., Berthou, S., Burke, E., Blockley, E., Carslaw, K., Dalvi, M., Edwards, J.,

Folberth, G. A., Gedney, N., Griffiths, P. T., Harper, A. B., Hendry, M. A., Hewitt, A. J., Johnson, B., Jones, A., Jones, C. D.,
1045   Keeble, J., Liddicoat, S., Morgenstern, O., Parker, R. J., Predoi, V., Robertson, E., Siahaan, A., Smith, R. S., Swaminathan,
R., Woodhouse, M. T., Zeng, G., and Zerroukat, M.: UKESM1: Description and Evaluation of the U.K. Earth System Model,
J. Adv. Model. Earth Syst., 11, 4513–4558, https://doi.org/10.1029/2019MS001739, 2019.

Seneviratne, S. I., Easterling, D., Goodess, C. M., Kanae, S., Kossin, J., Luo, Y., Marengo, J., McInnes, K., Rahimi, M.,
Reichstein, M., Sorteberg, A., Vera, C., and Zhang, X.: Changes in climate extremes and their impacts on the natural physical
1050   environment, in: Managing the Risks of Extreme Events and Disasters to Advance Climate Change Adaptation, edited by:
Field, C. B., Barros, V., Stocker, T. F., Qin, D., Dokken, D. J., Ebi, K. L., Mastrandrea, M. D., Mach, K. J., Plattner, G.-K.,
Allen, S. K., Tignor, M., and Midgley, P. M., A Special Report of Working Groups I and II of the Intergovernmental Panel on
Climate Change (IPCC), Cambridge, UK and New York, NY, USA, 109–230, https://doi.org/10.7916/d8-6nbt-s431, 2012.

Singer, M. B., Asfaw, D. T., Rosolem, R., Cuthbert, M. O., Miralles, D. G., MacLeod, D., Quichimbo, E. A., and Michaelides,
1055   K.: Hourly potential evapotranspiration at 0.1° resolution for the global land surface from 1981-present, Sci. Data, 8, 224,
https://doi.org/10.1038/s41597-021-01003-9, 2021.

Sonntag, D.: Important new values of the physical constants of 1986, vapor pressure formulations based on the ITS-90 and
psychrometric formulae, Zeitschrift fuer Meteorol., 70, 340–344, 1990.

Thuiller, W., Lavorel, S., Araújo, M. B., Sykes, M. T., and Prentice, I. C.: Climate change threats to plant diversity in Europe,
1060   Proc. Natl. Acad. Sci., 102, 8245–8250, https://doi.org/10.1073/pnas.0409902102, 2005.

Thuiller, W., Guéguen, M., Renaud, J., Karger, D. N., and Zimmermann, N. E.: Uncertainty in ensembles of global biodiversity
scenarios, Nat. Commun., 10, 1446, https://doi.org/10.1038/s41467-019-09519-w, 2019.

Weibull, W.: A Statistical Distribution Function of Wide Applicability, J. Appl. Mech., 18, 293–297,
https://doi.org/10.1115/1.4010337, 1951.

1065   Willis, K. J. and Bhagwat, S. A.: Biodiversity and Climate Change, Science (80-.)., 326, 806–807,
https://doi.org/10.1126/science.1178838, 2009.

WMO: Guide to Instruments and Methods of Observation, 8th ed., World Meteorological Organization, Geneva, 548 pp.,
2018.

Woodward, F. I.: Climate and plant distribution, Cambridge University Press, Cambridge, 192 pp., 1987.

1070   Yukimoto, S., Kawai, H., Koshiro, T., Oshima, N., Yoshida, K., Urakawa, S., Tsujino, H., Deushi, M., Tanaka, T., Hosaka,
M., Yabu, S., Yoshimura, H., Shindo, E., Mizuta, R., Obata, A., Adachi, Y., and Ishii, M.: The Meteorological Research
Institute Earth System Model Version 2.0, MRI-ESM2.0: Description and Basic Evaluation of the Physical Component, J.
Meteorol. Soc. Japan. Ser. II, 97, 931–965, https://doi.org/10.2151/jmsj.2019-051, 2019.

Zhang, K., Bosch-Serra, A. D., Boixadera, J., and Thompson, A. J.: Investigation of Water Dynamics and the Effect of
1075   Evapotranspiration on Grain Yield of Rainfed Wheat and Barley under a Mediterranean Environment: A Modelling Approach,
PLoS One, 10, e0131360, https://doi.org/10.1371/journal.pone.0131360, 2015.

Zhang, T.: Influence of the seasonal snow cover on the ground thermal regime: An overview, Rev. Geophys., 43,

https://doi.org/10.1029/2004RG000157, 2005.

Ziese, M., Rauthe-Schöch, A., Becker, A., Finger, P., Meyer-Christoffer, A., and Schneider, U.: GPCC Full Data Daily
1080 Version.2018 at 1.0°: Daily Land-Surface Precipitation from Rain-Gauges built on GTS-based and Historic Data,
https://doi.org/10.5676/DWD_GPCC/FD_D_V2018_100, 2018.

Zscheischler, J., Westra, S., van den Hurk, B. J. J. M., Seneviratne, S. I., Ward, P. J., Pitman, A., AghaKouchak, A., Bresch,
D. N., Leonard, M., Wahl, T., and Zhang, X.: Future climate risk from compound events, Nat. Clim. Chang., 8, 469–477,
https://doi.org/10.1038/s41558-018-0156-3, 2018.

1085